1    **Nuclear envelope assembly relies on CHMP-7 in the absence of BAF-LEM-mediated hole closure**

2

3    Sarah R. Barger[1], Lauren Penfield[2], Shirin Bahmanyar[1, #]

4

5    [1]Yale University, Department of Molecular, Cellular, Developmental Biology, 266 Whitney Ave., New

6    Haven, CT 06511

7    [2]Current address: Department of Molecular, Cellular, and Developmental Biology at University of

8    California, Santa Barbara, CA

9

10

11    [#]Correspondence: shirin.bahmanyar@yale.edu

12

**Abstract**

Barrier-to-autointegration factor (BAF) is a DNA binding protein that crosslinks chromatin to assemble the nuclear envelope (NE) after mitosis. BAF also binds the Lap2b-Emerin-Man1 (LEM) domain family of NE proteins to repair interphase ruptures. The NE adaptors to ESCRTs, LEMD2-CHMP7, seal NE holes surrounding mitotic spindle microtubules (MTs), but whether NE hole closure in mitosis involves BAF-LEM binding is not known. Here, we analyze NE sealing after meiosis II in *C. elegans* oocytes to show that BAF-LEM binding and LEM-2$^{LEMD2}$-CHMP-7 have distinct roles in hole closure around spindle MTs. LEM-2/EMR-1$^{emerin}$ function redundantly with BAF-1 to seal the NE. Compromising BAF-LEM binding revealed an additional role for EMR-1 in maintenance of the NE permeability barrier and an essential role for LEM-2-CHMP-7 in preventing NE assembly failure. The WH domain of LEM-2 recruits the majority of CHMP-7 to the NE in *C. elegans* and a LEM-2 -independent pool of CHMP-7, which is mostly enriched in the nucleoplasm, also contributes to NE stability. Thus, NE hole closure surrounding spindle MTs requires redundant mechanisms that safeguard against failure in NE assembly to support embryogenesis.

**Introduction**

The nuclear envelope (NE) is a domain of the endoplasmic reticulum (ER) that serves as a mechanically stable semi-permeable barrier to the genome (Ungricht and Kutay, 2017). The outer and inner nuclear membrane of the NE encase a lumen that is shared with the ER. The inner nuclear membrane (INM) has a unique protein composition and is associated with a meshwork of filamentous nuclear lamins. Each cell division, the NE and nuclear lamins disassemble to release mitotic chromosomes for capture by spindle microtubules (MTs). After chromosome segregation, the NE forms from ER-derived membranes. Assembly of nuclear pore complexes (NPCs) and closure of NE holes establish the NE permeability barrier. Failure in the barrier function of the NE can lead to DNA damage and disrupt genome regulation, highlighting the importance of understanding mechanisms that seal the NE after mitosis (Gauthier and Comaills, 2021; Rodriguez-Muñoz et al., 2022).

NE formation relies on the dsDNA binding protein, Barrier to Autointegration Factor (BAF), that dimerizes to crosslink DNA and bind to a subset of integral INM proteins and lamins (Sears and Roux, 2020). Immediately after exit from mitosis, dephosphorylation of BAF promotes its high affinity association with segregated chromosome masses (Ahn et al., 2019; Asencio et al., 2012; Marcelot et al., 2021; Snyers et al., 2018). BAF dimers bridge DNA segments to 'glue' individual chromosomes together (Samwer et al., 2017). Integral membrane LAP2-Emerin-MAN (LEM)-domain proteins bind to a groove at the BAF dimer junction through a conserved 40 amino acid 'LEM-domain' to tether associated ER membranes around the chromatin surface (Barton et al., 2015; Cai et al., 2007; Lin et al., 2000). Nascent nuclear membranes first wrap the exposed region of the segregated chromatin mass that is unoccupied by spindle microtubules (called the 'non-core' domain) (Liu and Pellman, 2020). The majority of NPCs assemble in the non-core domain to initiate nuclear transport.

After the initial phase of NE formation, BAF accumulates at the 'core' domain of the chromatin mass, which is the densely occupied by spindle MTs (Haraguchi et al., 2008). BAF recruits and concentrates LEM-domain proteins, including LEMD2 and emerin, to the core domain where NE sealing of holes occurs (Haraguchi et al., 2008; von Appen et al., 2020). The LEM-domain protein LEMD2 contributes to NE sealing through its C-terminal winged helix (WH) domain that directly binds and activates the conserved ESCRT-II/ESCRT-III hybrid protein CHMP7 (Gatta et al., 2021; Gu et al., 2017; von Appen et al., 2020). The WH of LEMD2 copolymerizes with CHMP7 to form 50-100 nm rings *in vitro* and it is thought that their assembly on the cytosolic surface of NE holes restricts diffusion of macromolecules (Gatta et al., 2021; von Appen et al., 2020). CHMP7 serves as the NE adaptor for downstream ESCRT-III membrane remodeling machinery including the spiral filament protein CHMP4B/VPS32 and the microtubule severing protein Spastin that coordinate spindle disassembly with fusion of small (<100 nm) NE holes (Vietri et al.,

60  2015; Ventimiglia et al., 2018; von Appen et al., 2020). Functions for other LEM-domain proteins at the
61  core domain are less well understood.

62      The essential role for BAF in NE assembly as well as the functional redundancy of multiple LEM-
63  domain proteins have made it challenging to test if BAF binding to LEM proteins serves a function aside
64  from downstream ESCRT recruitment. In mitotically dividing cells, expression of a dimerization mutant in
65  BAF, deficient in both DNA crosslinking and LEM-domain binding, results in hyper-micronucleation
66  where membranes wrap individual chromosomes because they are not crosslinked (Samwer et al., 2017).
67  Expression of a BAF mutant (BAF-L58R) that selectively prevents binding to LEM proteins did not cause
68  micronucleation, demonstrating that BAF-LEM binding is not essential for formation of a single nucleus;
69  however, whether sealing during NE formation is impaired in the absence of BAF-LEM binding was not
70  tested. Expression of BAF-L58R does not support repair of large holes that result from ruptures indicating
71  that BAF-LEM binding mediates NE sealing in interphase cells (Young et al., 2020). Importantly, CHMP7
72  accumulates at nuclear rupture sites but is not required for repair of ruptures (Halfmann et al., 2019). Thus,
73  in interphase, BAF-LEM binding has a distinct role from CHMP7 in NE sealing, particularly of large NE
74  holes that do not contain MTs (Halfmann et al., 2019; Young et al., 2020). Whether BAF-LEM binding and
75  CHMP7 have separate roles in sealing NE holes that surround spindle MTs in mitosis is not known.
76  Interestingly, LEMD2 binds MTs directly, which contributes to its enrichment at the core domain for NE
77  sealing in mitosis (von Appen et al., 2020), so there may be a separable function for LEMD2-CHMP7 from
78  BAF-LEM binding that depends on the presence of MTs.

79      Here, we take advantage of the opportunities provided by *C. elegans* to combine genetics and live
80  imaging to dissect the contributions of BAF to NE sealing and the relationship of sealing to successful
81  nuclear assembly. We focus on NE assembly after anaphase of meiosis II in fertilized oocytes to determine
82  the shared and unique functions for BAF, LEM-domain proteins and CHMP7 in sealing of the large hole
83  that surrounds spindle MTs, which establishes the permeability barrier in the first instance of NE formation
84  for the developing embryo (Penfield et al., 2020).

85      Our previous work defined the assembly dynamics of *C. elegans* LEM-2 (human LEMD2) and
86  presence of CHMP-7 (human CHMP7) at the micron-scale sized hole that surrounds the asymmetric
87  meiotic spindle (Penfield et al., 2020). Importantly, closure of the post-meiotic NE hole does not require
88  CHMP-7 (Penfield et al., 2020), but whether it requires the accumulation of membrane-bound LEM-domain
89  proteins was not known. The regulation and requirement for BAF (Ce BAF-1) in nuclear assembly is
90  conserved in *C. elegans* (Gorjanacz et al., 2007; Margalit et al., 2005). Furthermore, in contrast to human
91  cells that contain seven LEM-domain proteins, *C. elegans* contain only two integral membrane LEM-
92  domain proteins, EMR-1 (human emerin) and LEM-2, as well as a non-transmembrane containing LEM-
93  domain protein LEM-3 (human ANKLE1), none of which are essential genes (Barton et al., 2015; Lee et

94    al., 2000). Loss of both *lem-2* and *emr-1* results in embryonic lethality, which suggested that BAF-1
95    mediates its essential functions in nuclear assembly through redundant recruitment of these LEM-domain
96    proteins (Liu et al., 2003).

97         We introduced the conserved BAF-L58R separation-of-function mutation at the endogenous locus
98    of *C. elegans baf-1* to disrupt BAF-LEM binding. This mutant background allowed us to analyze the
99    contribution of BAF-LEM binding to NE sealing and assembly. Our work reveals that EMR-1 and LEM-2
100   function redundantly in binding to BAF-1 to facilitate NE sealing around spindle MTs. We demonstrate
101   that LEM-2-CHMP-7 are critical to stabilize the NE and safeguard against failure in NE assembly when
102   BAF-LEM binding is compromised. Our genetic studies further reveal unique functions for LEM-2 and
103   EMR-1 in maintenance of the NE permeability barrier and NE assembly. Thus, our work reveals redundant
104   and distinct roles for multiple key players in NE formation and dissects the relationship between NE sealing
105   and NE stability to support early embryonic development.

106

107   **Results**

108   **BAF-1 dynamics and regulation after chromosome segregation in meiosis II and mitosis**

109        Fertilization by haploid sperm triggers two rounds of meiosis in prophase I arrested *C. elegans*
110   oocytes to produce the haploid pronucleus as well as two extruded polar bodies (Fig. 1A, left; (Fabritius et
111   al., 2011)). The haploid oocyte-derived pronucleus forms as the acentriolar spindle elongates between
112   segregated chromosomes after anaphase II (Fig. 1A, right). The NE initially assembles on the side of
113   chromatin that is farthest from the acentriolar meiotic spindle and wraps around chromatin to form a sealing
114   plaque akin to the 'core domain' that surrounds persisting spindle microtubules in mitosis (Fig. 1A, 100s;
115   (Penfield et al., 2020)). The plaque condenses as the spindle dissipates (Fig. 1A, 200s) and then disperses
116   as the pronucleus rapidly expands (Fig. 1A, 400s). In contrast to the oocyte-derived pronucleus, the haploid
117   sperm-derived pronucleus, at the opposite end of the embryo, does not undergo closure of a large hole
118   around spindle microtubules (Fig. 1A, left). Thus, the fertilized *C. elegans* zygote provides the opportunity
119   to directly compare nuclear assembly with and without closure of a large hole around spindle microtubules
120   in a shared cytoplasm (Fig 1A; (Penfield et al., 2020)). Furthermore, analyzing the first instance of NE
121   formation allows us to eliminate confounding effects of prior rounds of failed NE assembly. Once formed,
122   the oocyte-derived and sperm-derived pronuclei meet at pseudocleavage (PC) regression and progress to
123   the first mitotic division (Fig. 1A; (Oegema, 2006)).

124        We generated a strain of *baf-1* tagged at its endogenous locus with mNeonGreen (mNG) and
125   3XFlag at the N-terminus ('mNG^BAF-1') to monitor BAF-1 dynamics at the sealing plaque. Embryo
126   production and viability were unaffected in this strain suggesting that the fusion protein does not
127   significantly interfere with BAF-1 function (Fig S1A). mNG^BAF-1 localizes on oocyte chromatin at

128   anaphase II onset and transitions to a bright focus at the sealing plaque as the adjacent meiotic spindle
129   lengthens and dissipates (Fig 1B, C). mNG^BAF-1 at the sealing plaque localized uniformly at the nuclear
130   rim ~400s following anaphase II onset (Fig 1B). mNG^BAF-1 associated with sperm chromatin
131   transitioned to a small focus that enriched along the nuclear rim with similar dynamics as the oocyte-derived
132   pronucleus (Fig. S1B; Movie 1). Thus, universal signaling mechanisms in the shared cytoplasm of the
133   fertilized oocyte triggered by anaphase II control BAF-1 dynamics on chromatin and the nuclear envelope.

134   The LEM-4-like protein (*lem-4*, human ANKLE-2) is an adaptor for PP2A that functions to
135   dephosphorylate BAF-1, which enhances its chromatin-association immediately after mitotic exit (Asencio
136   et al., 2012; Snyers et al., 2018; Marcelot et al., 2021) (Fig. S1C). Reducing *lem-4* by RNAi-depletion to
137   maintain BAF-1 in a phosphorylated state reduced mNG^BAF-1 accumulation at segregated meiotic
138   chromosomes (Fig. S1D) and delayed its accumulation on segregated mitotic chromosomes, as previously
139   reported (Fig S1E; (Asencio et al., 2012). Thus, LEM-4 likely regulates BAF-1 dynamics in meiosis II
140   similar to mitotically dividing cells.

141

142   **Enrichment of LEM-2 and EMR-1 at the sealing plaque in meiosis II requires BAF-1**

143   We tested whether BAF-1 controls the dynamics of LEM-2 and EMR-1 (emerin) at the reforming
144   NE and sealing plaque. We generated strains with *lem-2* and *emr-1* endogenously tagged with mNG using
145   CRISPR/Cas9 editing. LEM-2^mNG and mNG^EMR-1 dynamics to the nuclear rim and enrichment at the
146   sealing plaque were similar to mNG^BAF-1 and to prior reports for a LEM-2 transgene (Fig 1D and S1F;
147   (Penfield et al., 2020)). However, they did not accumulate at a sealing plaque in *baf-1* RNAi-depleted
148   embryos and instead membranes surrounded individual chromosomes that appeared condensed resulting in
149   a multi-lobed oocyte pronucleus (Fig 1D and S1F, Movie 2). Furthermore, the initial levels of LEM-2-
150   occupied membranes on chromatin during anaphase-II onset were significantly reduced in *baf-1* RNAi-
151   depleted embryos (Fig. 1D and S1G). The substantial ER-associated pool of mNG^EMR-1 made
152   comparable measurements unreliable (Fig. S1F). Embryos depleted of *baf-1* did not accumulate
153   GFP:Nuclear localization signal (NLS)-LacI in the nucleus, indicating a failure in NE sealing (Fig. 1E).
154   Thus, similar to penetrant RNAi-depletion of BAF in mammalian cells exiting mitosis (Samwer et al.,
155   2017), BAF-1 is necessary to form a single nucleus after meiosis II in *C. elegans*. Additionally, BAF-1
156   directs formation of the sealing plaque containing LEM-2 and EMR-1, which prompted us to use genetic
157   analysis to understand how BAF-1's recruitment of LEM-domain proteins contributes to sealing of the large
158   post-meiotic NE hole.

159

160   **A mutation in BAF-1 that prevents LEM-domain binding reduces its NE localization and is non-**
161   **essential in *C. elegans***

6

162    To understand the contribution of BAF-LEM binding in closure of the large hole that surrounds
163    meiotic spindle microtubules, we introduced mutations in conserved amino acid residues in *C. elegans baf-*
164    *1* that have been shown to serve as separation-of-function mutations in human BAF (Samwer et al., 2017;
165    Halfmann et al., 2019; Young et al., 2020; Fig 2A). BAF-G47E disrupts BAF dimerization and binding to
166    LEM-domain proteins while BAF-L58R selectively inhibits LEM-domain binding (Fig. 2A, B; (Halfmann
167    et al., 2019; Samwer et al., 2017; Young et al., 2020)).

168    We first introduced the mutations into RNAi-resistant *baf-1* transgenes to avoid embryonic lethality
169    and sterility that could result from significant disruption of *baf-1* function (Fig. S2A). RNAi-depletion of
170    *baf-1* caused 100% embryonic lethality (Fig. 2B), as expected (Gorjanacz et al., 2007; Margalit et al., 2005;
171    Zheng et al., 2000), and this was rescued in the presence of the WT re-encoded *baf-1* transgene, but not the
172    dimerization deficient *baf-1(G47E)* mutant transgene (Fig. 2B). The *baf-1(L58R)* mutant re-encoded
173    transgene supported viability in *baf-1* RNAi-depleted embryos (Fig. 2B). We therefore introduced the *baf-*
174    *1(L58R)* mutation at the endogenous locus (Fig. S2B). The *baf-1(L58R)* mutant worm expressed normal
175    levels of BAF-1 protein (Fig. S2C), did not cause embryonic lethality, and resulted in a slight reduction in
176    brood size (Fig. S2D). Together these data indicate that BAF-LEM binding is not essential for germline
177    development or embryogenesis.

178    We next tested if BAF-LEM binding is required for BAF-1 localization at the INM. BAF localizes
179    to both the nucleoplasm and INM; LEM-domain proteins bind BAF at the INM (Haraguchi et al., 2007;
180    Liu et al., 2003), so we expected to observe reduced BAF-1-L58R mutant protein at the NE, but not the
181    nucleoplasm (Halfmann et al., 2019; Samwer et al., 2017; Young et al., 2020). In the 1-cell stage embryo,
182    mNG^BAF-1 is enriched at the NE of the oocyte- and sperm-derived pronuclei, and localizes to the
183    nucleoplasm, ER, and diffusely in the cytoplasm (Fig. 2C). Our attempts to homozygous a *baf-1(L58R)*
184    mutant animal tagged at the endogenous locus with mNG were unsuccessful suggesting that the mNG tag
185    together with the L58R mutation compromise BAF-1 function at the organismal level. To bypass this issue,
186    we quantified the NE and nucleoplasmic fluorescence signal of heterozygous embryos carrying one copy
187    of mNG tagged *baf-1* and one untagged copy of wild type *baf-1* (Fig. 2C-F). In heterozygous wild type
188    mNG^ *baf-1* / *baf-1* embryos, the NE and nucleoplasmic mNG fluorescence signal was approximately half
189    that of the homozygous mNG tagged wild type *baf-1* strain (Fig. 2C, D). The NE to nucleoplasmic ratio of
190    the mNG fluorescence was the same in both homozygous and heterozygous strains, so even with half the
191    amount of protein the proportion of wild type BAF-1 at the NE versus the nucleoplasm remains constant
192    (Fig. 2F).

193    Both the NE and nucleoplasmic mNG fluorescence levels were significantly lower in heterozygote
194    mNG^*baf-1*(L58R)/ *baf-1* than in wild type mNG^*baf-1*/*baf-1* embryos (Fig. 2E), although protein levels
195    of untagged BAF-1-L58R in the *baf-1(L58R)* mutant strain that we use throughout this study are unchanged

196    (Fig. S2C). The lower NE:nucleoplasmic ratio reflected a greater decrease of the mNG^BAF-1-L58R

197    mutant protein at the NE than nucleoplasm (Fig. 2E, F). The faint mNG^BAF-1-L58R localization at the

198    nuclear rim may be through dimerization with untagged wild type BAF-1 or through association with the

199    nuclear lamina or an unidentified NE adaptor (Holaska et al., 2003; Kono et al., 2022; Samson et al., 2018).

200    ER-localized signal was also lost in mNG^ *baf-1*(L58R)/ *baf-1* heterozygote embryos indicating that BAF-

201    1 associates with the ER through binding to LEM domain proteins (Fig. 2E). Reduced nuclear rim, but

202    unchanged nucleoplasmic signal, of mNG^BAF-1 in *emr-1Δ* embryos, as reflected in the lower

203    NE:nucleoplasmic ratio (Fig. 2C, D), is consistent with past findings that emerin contributes to BAF-1

204    binding at the INM (Asencio et al., 2012). We were unable to assess the localization of mNG^BAF-1-L58R

205    upon loss of *lem-2* because of the synergistic sterility phenotype that results from this genetic background

206    (see below Fig. 2G). Together, we conclude that the *C. elegans* BAF-1-L58R mutant is compromised in its

207    NE-association, as previously shown for the mutant human BAF homologue (Halfmann et al., 2019;

208    Samwer et al., 2017; Young et al., 2020), and that multiple LEM-domain proteins recruit BAF-1 to the

209    INM.

210

211    **Distinct functions for LEM proteins in embryo and germline development revealed by the *baf-***

212    ***1(L58R)* mutant**

213          We crossed the *baf-1(L58R)* strain to deletion alleles in each of the three *C. elegans* LEM-domain

214    genes (*emr-1, lem-2,* and *lem-3*) because we predicted that if LEM proteins have redundant or related

215    functions to BAF-LEM binding, then a double mutant (e.g. *emr-1Δ; baf-1(L58R))* would result in

216    synergistic phenotypes (e.g. increased lethality). Alternatively, if LEM proteins function only through

217    binding to BAF-1, then a double mutant with *baf-1(L58R)* would not cause a significant increase in

218    embryo viability or production.  Deletion of *emr-1* or a *lem-3* mutant allele with reduced function in the

219    *baf-1(L58R)* mutant strain resulted in only a slight decrease in brood size and embryonic viability (Fig.

220    2G, H) suggesting that these LEM proteins do not have a function that is redundant with BAF-LEM

221    binding to support embryo and germline development. In contrast, deletion of the *lem-2* gene locus did

222    not cause lethality or sterility on its own (Fig. 2G, H) but the *lem-2Δ*; *baf-1(L58R)* double mutant

223    inhibited germline development resulting in sterility in 100% of worms (Fig. 2G, S2I). Note that we

224    found an annotation error in the *lem-2(tm1582)* mutant allele, which has been widely used and interpreted

225    as a *lem-2* deletion strain (Barkan et al., 2012; Bone et al., 2014; Dittrich et al., 2012; González-Aguilera

226    et al., 2014; Harr et al., 2020; Morales-Martínez et al., 2015; Penfield et al., 2020; Shankar et al., 2022),

227    in which the 3' region that encodes for the WH domain is intact (Fig. S2F) (Davis et al., 2022). We

228    therefore generated a CRISPR-Cas9 gene edited strain that deletes the entire *lem-2* gene locus for this

229    study (Fig. S2G, H). Together, these data indicate that LEM-2, but not EMR-1 or LEM-3, has a redundant

8

230  function to BAF-LEM binding in germline development, and further verify that the BAF-1-L58R mutant

231  protein is functionally compromised.

232

233  **Abnormal dynamics of endogenously tagged LEM-2 and EMR-1 at the reforming NE and sealing**

234  **plaque in *baf-1(L58R)* mutants**

235      We next tested whether compromising BAF-LEM protein interactions impacted the recruitment

236  of endogenous LEM-2^mNG and EMR-1^mNG to the reforming post-meiotic NE (Fig. 3, Fig S3A).

237  LEM-2^mNG appeared on the nascent NE at anaphase II onset at lower levels in *baf-1(L58R)* mutant

238  embryos compared to control embryos (Fig. 3A, B, Movie 3), similar to *baf-1* depletion (Fig. S1G).

239  Instead of the organized sealing plaque that forms directly adjacent to the meiotic II spindle under control

240  conditions (100s, Fig. 3A), LEM-2^mNG formed smaller foci around condensed chromatin that coalesced

241  into a single punctum with lower fluorescence intensity levels and delayed appearance in *baf-1(L58R)*

242  mutants compared to controls (Fig. 3C-D). Furthermore, the punctum of LEM-2^mNG in *baf-1(L58R)*

243  mutant oocytes persisted ~ 300s longer than the sealing plaque in control embryos (Fig. 3E). Fully formed

244  oocyte-derived pronuclei in *baf-1(L58R)* mutant contained lower levels of LEM-2^mNG at the NE (Fig.

245  S3B, C) despite equal levels of global LEM-2 protein (Fig S3D). Similar observations were made for

246  mNG^EMR-1 dynamics in *baf-1(L58R)* mutants (Fig. 3F, Fig. S3B, C). Additionally, compromised BAF-

247  LEM binding resulted in delayed LEM-2^mNG on nascent nuclear membranes following the first mitotic

248  division that did not fully enrich at the 'core' domain (Fig. S3E-G). Together, these data confirm that

249  BAF-1 recruits and organizes LEM proteins to the sealing plaque through its BAF-LEM domain binding

250  function. The fact that LEM-2 and EMR-1 can localize to the NE independent of BAF-1 binding, albeit at

251  significantly lower levels (Fig S3B, C), supported the possibility that these proteins have functions

252  independent of BAF-1-mediated recruitment at the NE.

253

254  **LEM-2 and EMR-1 compensate for each other in binding to BAF-1 to seal the NE around spindle**

255  **MTs**

256      We compared NE assembly and sealing in the oocyte versus sperm-derived pronuclei to determine

257  if there is a unique requirement for BAF-LEM binding in closure of the large NE hole surrounding spindle

258  MTs (Fig. 4). Live imaging of a general ER marker (SP12:GFP) and chromosomes (mCh:Histone(H2B)

259  showed that 100% of both oocyte and sperm-derived pronuclei RNAi-depleted of *baf-1* are multi-lobed

260  (Fig. 4B), while in *baf-1(L58R)* mutants a proportion of oocyte- but not sperm-derived pronuclei were

261  malformed and had faint intranuclear membranes (Fig. 4A, B). Reducing *lem-4* levels to prevent

262  dephosphorylation of BAF-1 mildly impacted nuclear shape on its own (Fig. 4B), but resembled a penetrant

263  BAF-1 depletion in *baf-1(L58R)* mutants, which was specific to the oocyte-derived pronucleus (Fig. 4A, B,

264   Movie 4). These data indicate that there is a greater reliance on BAF-LEM binding for nuclear formation

265   when a large hole that surrounds spindle microtubules must be sealed. Nuclear formation in mitotic *baf-1-*

266   *L58R* embryos was delayed and resulted in smaller nuclei (Fig. S4A, B) suggesting that BAF-LEM binding

267   contributes to NE assembly in both meiosis and mitosis in *C. elegans*.

268       We next monitored the time course of nuclear import of a GFP:NLS reporter following anaphase

269   II onset to PC regression in both the oocyte and sperm-derived pronuclei in *baf-1(L58R)* mutant embryos

270   (Fig. 4C, S4C). The nuclear to cytoplasmic ratio of the GFP:NLS reporter directly following nuclear

271   formation in the oocyte-derived, but not in the sperm-derived pronucleus, was significantly lower in *baf-*

272   *1(L58R)* embryos compared to wild type embryos (Fig 4C, Fig. S4C). Furthermore, nuclear exclusion of

273   GFP:α tubulin, which is actively exported from pronuclei (Hayashi et al., 2012) and serves as an indicator

274   of closure of large NE holes (Penfield et al., 2020), was delayed, but not inhibited, in the *baf-1(L58R)*

275   mutant oocyte-derived pronucleus (Fig 4D, E). Together, these data indicate that the timely closure of the

276   large NE hole surrounding meiotic spindle MTs requires the ability of BAF to bind LEM proteins.

277       Deletion of *lem-2* did not impact the initial rate of nuclear import (Fig. 4C) nor nuclear assembly

278   (Fig. S4D, E) following anaphase II, although the nuclear GFP:NLS signal did not reach the maximum

279   wild type levels in these mutant embryos suggesting that LEM-2 may have a parallel function that in

280   addition to binding to BAF-1 is required for maintenance of the NE permeability barrier. Sterility

281   resulting from loss of *lem-2* in *baf-1(L58R)* worms prevented us from genetically testing the

282   consequences on nuclear sealing resulting from loss of *lem-2* in *baf-1(L58R)* embryos.

283       Deletion of *emr-1* resulted in lower retention of nuclear GFP:NLS (Fig. S4D, E; Fig. 4C), similar

284   to loss of *lem-2*. In *baf-1-L58R* pronuclei, RNAi-depletion of *emr-1* resulted in ~42% of oocyte-derived

285   containing nuclear GFP:α-tubulin at PC regression (Fig. 4E), suggesting that EMR-1 has an additional

286   function to BAF-1 in stabilizing the NE barrier when NE sealing around spindle MTs is required. Both

287   oocyte- and sperm-derived pronuclei were permeable to GFP:α-tubulin at PC regression upon RNAi-

288   depletion of *lem-4* in the *baf-1(L58R)* mutant, further supporting the general requirement for both

289   chromatin binding and LEM domain binding functions of BAF-1 to support stable nuclear assembly (Fig.

290   4A, B, E).

291       We conclude that LEM-2 and EMR-1 compensate for each other in binding to BAF-1 to ensure

292   NE sealing around spindle MTs - loss of either gene alone results in milder defects in NE sealing than in

293   the *baf-1(L58R)* mutant. Our data also reveal that there are unique functions for LEM-2 and EMR-1 that

294   are distinct from BAF-LEM binding. EMR-1 has a parallel function to BAF-LEM binding required for

295   maintenance of the NE barrier. The sterility phenotype that is specific to loss of *lem-2* in the *baf-1(L58R)*

296   mutant indicates a unique function for LEM-2 from EMR-1 in germline development that is redundant to

297   BAF-LEM binding.

**Nuclear envelope assembly around spindle MTs relies on CHMP-7 when BAF-LEM binding is compromised**

The mild NE assembly defects and delayed but not failed sealing in the absence of BAF-LEM binding prompted us to test for other factors that may be functioning redundantly to prevent catastrophic loss of the NE permeability barrier. Our data showing that LEM-2 and EMR-1 are recruited to the NE even in the absence of BAF-LEM binding suggested that downstream ESCRT-mediated NE remodeling may support NE formation under these conditions. Furthermore, evidence in *C. elegans* suggests that CHMP-7 contributes to NE sealing and stability under conditions of increased lipid biogenesis or a weakened nuclear lamina (Penfield et al., 2020; Shankar et al., 2022). We did not detect defects in formation of the oocyte and sperm-derived pronuclei in embryos deleted for *chmp-7* (Fig. 5A, B), similar to our past results (Penfield et al., 2020). In contrast, in ~35% of *chmp-7Δ*; *baf-1(L58R)* double mutant embryos the oocyte-, but not sperm-, derived pronucleus appeared lobed (Fig. 5A, B and see also Fig. S5A). These NE assembly abnormalities led to ~47% of *chmp-7Δ*; *baf-1(L58R)* embryos containing collapsed oocyte-derived pronuclei at pronuclear meeting, whereas sperm-derived pronuclei appeared normal (Fig. S5A, Movie 5). Approximately half of *chmp-7Δ*; *baf-1(L58R)* embryos do not survive to hatching (Fig. 5C), which is reflected in the severe mitotic defects observed in these mutants that appeared to compound with subsequent cell divisions (Fig. S5B). The enhanced phenotypes are specific to loss of *chmp-7* in the *baf-1(L58R)* mutant background in which both EMR-1 and LEM-2 binding to BAF-1 are compromised because *chmp-7Δ*; *emr-1Δ* and *chmp-7Δ*; *lem-2Δ* mutant embryos are mostly viable (Fig. 5C) further indicating that binding of BAF-1 to EMR-1 and LEM-2 functions redundantly to promote hole closure.

While some *chmp-7Δ*; *baf-1(L58R)* oocyte-derived pronuclei assembled into a normal shape (Fig. 5A, B, ~19% "circular"), they did not establish or maintain nuclear accumulation of the GFP:NLS reporter (Fig. 5D). Furthermore, the majority (94%) of these pronuclei failed to exclude GFP:α-tubulin (Fig. 5E, S5C). Thus, CHMP-7 is required for successful, albeit delayed, establishment of the NE permeability barrier when BAF-LEM-domain binding is impaired. The fact that oocyte-derived pronuclei sometimes assemble under these conditions and ~47% of embryos survive to hatching (Fig. 4C) suggests that the likelihood of NE assembly failure may depend on the extent of loss of the NE permeability barrier and stability of the NE hole. Together, these data show that CHMP-7 protects against failure in the NE barrier when NE hole closure around spindle MTs is defective.

**BAF-LEM binding controls the levels and dynamics of CHMP-7 during NE formation and sealing**

To understand how CHMP-7 contributes to normal NE sealing and assembly in the absence of BAF-LEM binding, we first monitored the levels, dynamics and organization of endogenously tagged GFP^CHMP-7 at the reforming NE and sealing plaque after anaphase II onset. CHMP-7 is constitutively

11

332 localized to the nuclear rim and in the nucleoplasm in *C. elegans* embryos (Shankar et al., 2022). In

333 control embryos, nuclear rim-associated CHMP-7 appears during anaphase II onset, wraps around

334 chromatin and enriches at the sealing plaque, similar to LEM-2 (Fig. 5F). GFP^CHMP-7 accumulates in

335 the nucleoplasm ~200s after anaphase II onset, concomitant with establishment of the nuclear

336 permeability barrier (Fig. 5F, Movie 6). In the *baf-1(L58R)* mutant, GFP^CHMP-7 levels were initially

337 lower at the nuclear rim (0s, Fig. S5D) and discrete CHMP-7 foci formed around condensed chromatin

338 (Fig. 5F, 200 s), which coalesced into a disorganized focus rather than a distinct plaque (Fig. 5F). CHMP-

339 7 also localized to the intranuclear membranes observed in assembled oocyte pronuclei of *baf-1(L58R)*

340 mutant (400s, Fig. 5F). Lower levels and abnormal dynamics of GFP^CHMP-7 were also observed

341 during NE formation in mitotic embryos of the *baf-1(L58R)* mutant (Fig. S5E, F), similar to LEM-

342 2^mNG.

343     Thus, the localization and dynamics of endogenous CHMP-7 at the reforming NE after meiosis II

344 and mitosis resembles that of LEM-2 and EMR-1 and is consistent with the role of BAF-1 in recruiting

345 and organizing LEM-domain proteins that then regulate CHMP-7 localization and dynamics. However,

346 the enhanced severity of *chmp-7Δ*; *baf-1(L58R)* suggested that CHMP-7 functions independently of BAF-

347 LEM binding to ensure NE sealing and assembly.

348

349 **LEM-2-dependent and independent pools of CHMP-7 contribute to post-meiotic NE assembly**

350     CHMP-7 localizes to the NE in *baf-1(L58R)* mutants during reformation, albeit in a reduced and

351 disorganized manner at initial timepoints, indicating recruitment of CHMP-7 to the NE is only partially

352 dependent on BAF-LEM binding. Prior work had suggested that both LEM-2 and EMR-1 are redundantly

353 required for CHMP-7 localization to the INM in *C. elegans* (Shankar et al., 2022); however, the

354 misannotated *lem-2* mutant allele strain was used assess CHMP-7 dynamics (see Fig. S2F). We found that

355 nuclear rim localization of GFP^CHMP-7 was not detectable in the CRISPR-Cas9 gene edited *lem-2Δ*

356 strain (Fig. 6A). GFP^CHMP-7 localization to the ER in mitotically dividing cells was also abolished in

357 *lem-2Δ* embryos (Fig. S6A). Deletion of the WH domain of *lem-2* using CRISPR-Cas9 gene editing

358 further revealed that the WH of LEM-2 is responsible for recruiting CHMP-7 to the nuclear rim, similar

359 to other systems (Fig. 6A) (Gu et al., 2017; von Appen et al., 2020). Deletion of *emr-1* in this genetic

360 background did not result in a change in GFP^CHMP-7 localization (Fig 6A). Thus, LEM-2 is required to

361 retain the majority of CHMP-7 at the INM in *C. elegans* embryos. We did observe a very slight nuclear

362 rim fluorescence signal of GFP^CHMP-7 in *lem-2Δ* and *lem-2-ΔWH* mutants ~160-180s after anaphase II

363 onset in meiosis and anaphase onset in mitosis (Fig. 6B, S6C) indicating that some CHMP-7 can associate

364 with the nuclear rim without LEM-2, which may be EMR-1-dependent.  Neither LEM-2 nor EMR-1 are

365 necessary for nuclear accumulation of CHMP-7 (Fig. 6A) and we observed increased nuclear

12

366    GFP^CHMP-7 levels in *lem-2Δ* and *lem-2 ΔWH* oocyte-derived pronuclei (Fig. S6B). This suggested that

367    the CHMP-7 pool that doesn't localize to the nuclear rim in the absence of LEM-2 binding accumulates in

368    the nucleoplasm. Together, these data demonstrate that the LEM-2 WH domain recruits CHMP-7 to the

369    NE even in the absence of BAF-LEM binding, which may explain why CHMP-7 can compensate for

370    defective NE sealing in the *baf-1(L58R)* background.

371           We next tested whether the LEM-2 independent pool of CHMP-7 that is mostly nuclear-enriched

372    can function to support nuclear assembly. Nuclear GFP^CHMP-7 accumulates during post-meiotic and

373    mitotic NE formation, but fails to enrich at the sealing plaque or 'core' domain without LEM-2 (Fig. 6B,

374    S6C, Movie 7). To test if the LEM-2-independent pools of CHMP-7 are functional in NE assembly, we

375    monitored NE formation in *lem-2-ΔWH; baf-1(L58R)* double mutant embryos (Fig. 6C). A lower

376    percentage of *lem-2-ΔWH; baf-1(L58R)* double mutant embryos displayed lobed oocyte-derived pronuclei

377    (~13%; Fig. 6C, D) compared to *chmp-7Δ; baf-1(L58R)* double mutants (see Fig. 5B) suggesting the pool

378    of CHMP-7 is partially functional in NE formation when not bound to LEM-2. Furthermore, the

379    incidence of oocyte pronuclear collapse and embryonic lethality was significantly reduced in the *lem-2*

380    *ΔWH; baf-1(L58R)* mutants as compared to *chmp-7Δ; baf-1(L58R)* mutants (Fig. 6E, F). Together, these

381    data reveal that LEM-2-independent pools of CHMP-7 contribute to NE formation and suggest that a

382    nucleoplasmic pool of CHMP-7 may be functional in nuclear assembly in *C. elegans*.

## Discussion

We demonstrate that BAF-1 binding to LEM-domain proteins determines the position and timing of LEM-2/EMR-1 and CHMP-7 assembly at the 'sealing plaque,' which forms the core domain of the NE adjacent to spindle MTs in fertilized *C. elegans* oocytes. We show that NE hole closure around spindle MTs does not depend on LEM-2, EMR-1 or CHMP-7 on their own, but BAF binding to LEM-2 and EMR-1 functions redundantly to enable hole closure. Our genetic analysis also revealed unique functions for LEM-2 and EMR-1 aside from binding to BAF-1 in NE stability and germline development. We demonstrate that CHMP-7 becomes essential to formation of the NE permeability barrier and embryonic viability in the absence of BAF-LEM domain binding. Both LEM-2 dependent and independent pools of CHMP-7 contribute to this essential function. Thus, multiple redundant mechanisms exist to prevent failure in post-meiotic NE assembly, which is essential for early embryo development.

We propose that BAF-mediated recruitment of LEM proteins and associated membranes resolves large gaps in the core domain of the NE that is obstructed by spindle microtubules while CHMP-7 functions with LEM-2 to stabilize the NE against failure in hole closure (Fig. S6D, top panel). Our prior work showed that limiting membrane biogenesis ensures successful post-meiotic hole closure (Penfield et al., 2020; Barger et al., 2022), providing further evidence that membrane feeding to narrow and close holes may be regulated to establish the NE permeability barrier. The function for BAF-LEM binding in post-meiotic hole closure is similar to its role in repair of interphase ruptures that do not contain MTs but are also micron-scale sized (Halfmann et al., 2019; Young et al., 2020). *In vitro* cross-linked BAF can exclude large macromolecules (Samwer et al., 2017) and it's possible that BAF-LEM interactions further serve to plug large NE holes to promote sealing. Our data reveals an additional requirement for LEM-2/CHMP-7 when spindle MTs are present to stabilize the NE. Our genetic analysis also shows that different LEM-domain proteins serve distinct functions in NE assembly that are independent but partially redundant with BAF-LEM binding. How BAF-LEM interactions are further regulated by BAF phosphorylation during NE sealing and assembly requires further study.

The LEM-2 winged helix (WH) domain activates CHMP-7 to promote its ESCRT-III polymerization *in vitro* (Gatta et al., 2021; von Appen et al., 2020). However, neither LEM-2 nor CHMP-7 are required for closure of the large post-meiotic NE hole on their own (Penfield et al., 2020). LEM-2/CHMP-7 assembly may instead provide a fallback mechanism that stabilizes the NE hole should NE sealing fail (Fig. S6D). A role for CHMP-7 in restricting NE hole size has recently been suggested for NE sealing following spindle pole body extrusion in *S. pombe* (Ader et al., 2022). It is also possible that LEM-2/CHMP-7 restrict uncoordinated membrane feeding or remodel abnormal membranes at the core region that otherwise make NE assembly vulnerable to failure, especially with presence of a large hole and spindle MTs. Evidence in mammalian cells and budding yeast suggests that improper activation and mislocalization

14

417    of CHMP7 can lead to harmful nuclear membrane deformations (Thaller et al., 2019; Vietri et al., 2020).

418    Thus, the disorganized assemblies of core proteins that we observed in the absence of BAF-LEM domain

419    binding may not only be perturbed in function for sealing, but also deleterious to NE formation. We also

420    cannot eliminate the possibility that the BAF-L58R mutant may retain some binding to LEM domain

421    proteins, although the accumulation of LEM domain proteins at the NE is significantly reduced.

422    Nevertheless, our genetic evidence showing that loss of CHMP-7 exacerbates phenotypes in the BAF-L58R

423    mutant suggest that these assemblies or other pools of CHMP-7 (see below) protect against assembly

424    failure.

425        In *C. elegans,* CHMP-7 is constitutively localized in the nucleoplasm and at the INM in fully

426    formed nuclei (Shankar et al., 2022). This localization is unlike CHMP7 in budding yeast and mammalian

427    cells in which it is cytoplasmic or ER-associated, respectively, and thus physically segregated from LEM-

428    2 presumably in an inactive form (Bauer et al., 2015; Gatta et al., 2021; Olmos et al., 2016; Thaller et al.,

429    2019). CHMP7 is excluded from the nucleus in these systems through a conserved nuclear export signal

430    and activated when it gains access to the LEM-2 WH in mitosis and upon loss of NE integrity in

431    interphase (Gatta et al., 2021; Thaller et al., 2019; Vietri et al., 2020). The fact that CHMP-7 is

432    constitutively nuclear-enriched and accessible to LEM-2 in *C. elegans* highlights that there may be

433    alternative mechanisms that activate this complex upon loss of NE integrity or that cytoplasmic CHMP-7

434    in *C. elegans* may be specifically primed for this function.  When we generated a deletion allele in *lem-2*,

435    we discovered that LEM-2 is required for the majority of CHMP-7 to associate with the INM in *C.*

436    *elegans*. Thus, LEM-2/CHMP-7 may be co-polymerized at the INM in *C. elegans* after NE sealing, but

437    limited in the ability to recruit downstream ESCRTs.

438        We found that a LEM-2-WH-independent pool of CHMP-7 partially supports NE assembly (Fig.

439    S6D, bottom panels). Prior work showed that CHMP7 binds peripherally to membranes through a

440    hydrophobic patch that in budding yeast resembles an amphipathic helix (AH) and this association is

441    necessary for its function (Olmos et al., 2016; Thaller et al., 2021). Prediction algorithms were unable to

442    identify a reliable AH in a similar region for *C. elegans* CHMP-7 where a stretch of hydrophobic residues

443    exist. Whether the nuclear or minor nuclear rim pool of CHMP-7 is the functional pool that partially

444    supports NE assembly is unclear. Interestingly, aberrant nuclear accumulation of CHMP7 is associated

445    with diseased neurons from patients with ALS (amyotrophic lateral sclerosis) and reduces NPC levels

446    (Coyne et al., 2021). There may be aspects of *C. elegans* CHMP-7 that allow for it to remain inactive

447    when soluble in the nucleus or for it to perform a unique function when unbound to membranes.

448        It is surprising that some oocyte-derived pronuclei assemble in the absence of both BAF-LEM

449    domain binding and CHMP-7 even with a defective nuclear permeability barrier. This suggests that

450    nuclear assembly is prone to failure at a stochastic rate that may depend on whether the timing of

15

451     dissolution and detachment of spindle MTs is synchronized with the local stability of the NE hole. These

452     NE irregularities sometimes prevent nuclear assembly or allow assembly of nuclei that later collapse. Our

453     genetic experimental system of *C. elegans* allowed us to quantitively analyze NE sealing and monitor its

454     impact on nuclear assembly and embryonic survival. Together, the redundant mechanisms that support

455     NE assembly made evident in this study emphasize the robust nature of NE formation that is required for

456     early development.

457

458     **Acknowledgments**

464

465     **Competing interests**

466     The authors declare no competing or financial interests.

467

468     **Author Contributions**

469     Conceptualization: S.R.B, S.B ; Methodology: S.R.B, L.P.; Validation: S.R.B.; Formal analysis: S.R.B.;

470     Investigation: S.R.B; Resources: S.R.B, L.P.; Data curation: S.R.B.; Writing - original draft: S.R.B, S.B;

471     Writing – review & editing: S.R.B, L.P., S.B. ; Visualization: S.R.B.; Supervision: S.B.; Project

472     administration: S.R.B, S.B; Funding acquisition: S.R.B, S.B.

473

474     **Funding**

477

478     **Data availability**

479     Almost all relevant data can be found within the article and its supplementary information. Further

480     requests for data or reagents can be made to the corresponding author. CRISPR-Cas9 edited strains will

481     be deposited in the CGC.

482
483     **Materials and Methods**
484

485     **Strain maintenance and generation**

486    The *C. elegans* strains used in this study are listed in Table S1. Strains were maintained at 20°C on nematode

487    growth media (NGM) plates seeded with OP-50 *Escherichia coli.* The original MosSCI strain was

488    maintained at 15°C.

489

490    *MosSCI strains*

491    The re-encoded *baf-1* transgene was cloned into pCFJ151 for integration into the Mos1 site on Chromosome

492    I (MosSCI; (Frøkjaer-Jensen et al., 2008)). Mutagenesis was performed using the primers listed in Table

493    S2. Injection mixes contained the following: *baf-1* transgene-containing plasmid (10 ng/μl), a plasmid

494    encoding the Mos1 transposase (Pglh- 2::transposase, pJL43.1, 10 ng/μl), and three plasmids encoding

495    fluorescent co-injection markers: Pmyo-2::mCherry (pCFJ90, 1.4 ng/μl), Pmyo- 3::mCherry (pCFJ104, 2.9

496    ng/μl), and Prab-3::mCherry (pGH8, 5.7 ng/μl). Injection mix was spun down (15,000 rpm, 15 minutes,

497    4°C) to remove particulates. Young adult hermaphrodites (EG8078) were injected and singled onto OP50

498    seeded plates for recovery. After ~7-10 days, non-*unc* progeny lacking fluorescent markers were isolated

499    and screened for transgene integration by PCR.

500

501    *CRISPR-Cas9 deletion strains*

502    The deletion for *lem-2* (W01G7.5) was generated using two CRISPR guides "crRNA", which were chosen

503    using IDT's custom CRISPR guide algorithm (See Figure S1G). Individually, 1 μl of the purified crRNAs

504    were annealed to 1 μl of trans-activating crRNA (tracrRNA) by incubating RNAs at 95°C for 5 minutes. A

505    dpy-10 crRNA was used for co-CRISPR selection. An injection mix with the following components was

506    set up at room temperature and incubated for 5 minutes: *lem-2* crRNA-1 (11.7 μM), *lem-2* crRNA-2 (11.7

507    μM), purified Cas9-NLS protein (qb3 Berkeley, 14.7 μM), *dpy-10* guide (3.7 μM). Finally, a *dpy-10* repair

508    template (29 ng/mL) (Paix et al., 2015) was added and the mix was spun down (15,000 rpm) for 30 minutes

509    at 4°C. The RNA-protein mix was injected into the gonads of N2 young adult worms, which were allowed

510    to recover for three days. F1 progeny with a roller phenotype were singled out to individual plates. After

511    three days, F1 mothers were genotyped by PCR. The deletion strain was sequenced and outcrossed six times

512    to N2 worms before use and characterization.

513

514    *CRISPR-Cas9 fluorescent knock-in strains*

515    Fluorescent endogenous tagging of *baf-1, lem-2 and emr-1* was performed using a self-excising cassette

516    (SEC) repair template (Dickinson and Goldstein, 2016; Hastie et al., 2019) (see Fig. S2E & S3A).

517    Homology arms (500-800bp) were cloned into the SEC vectors (pDD268). Unique sgRNAs were cloned

518    into the Cas9 guide plasmid pDD122 (Addgene, #47550). Following sequencing, injection plasmids were

519    miniprepped using PureLink HiPure Plasmid Miniprep Kit (Thermo Fisher Scientific). Plasmids were

520 combined at 100 ng/µl SEC plasmids and 50 ng/µl Cas9 plasmid and spun down (15,000 rpm) for 30

521 minutes at 4°C. Young adult N2 worms were injected and rescued to individual plates to recover for three

522 days at 25°C. Plates were screened for roller progeny and positive plates were treated with approximately

523 200-300 µl of hygromycin B (20 mg/mL) (Thermo Fisher Scientific). Hydromycin-resistant roller worms

524 were singled to individual plates to assess roller progeny. Plates that had roller progeny were heat-shocked

525 at 34°C for 4 hours and allowed to recover at 20°C. Non-roller worms were singled to individual plates and

526 progeny were screened for fluorescent protein integration by microscopy. Knock-in worms were sequence-

527 confirmed and outcrossed four times to N2 worms.

528

529 **RNAi**

530 Primers were designed using Primer3T to amplify a 200-1000 bp region of the gene of interest (see Table

531 S2) using N2 gDNA as a template. The amplicon was then column purified and reversed transcribed using

532 a T7 enzyme (MEGAscript, Life Technologies). The synthesized RNAs were purified using phenol-

533 chloroform and resuspended in 1X soaking buffer (32.7 mM $Na_2HPO_4$, 16.5 mM $KH_2PO_4$, 6.3 mM NaCl,

534 14.2 mM $NH_4Cl$). RNA reactions were annealed at 68°C for 10 minutes followed by 37°C for 30 minutes.

535 dsRNAs were brought to a final concentration of ~2000 ng/µl and stored as 2-µl aliquots at –80°C. For each

536 experiment, a fresh aliquot was diluted to ~1000 ng/µl using 1X soaking buffer and centrifuged at 15,000

537 rpm for 30 minutes at 4°C. 0.35µl of the diluted dsRNA was loaded into the back of a pulled capillary

538 needle and injected into the gut of L4 worms. Injected worms were rescued to plates seeded with OP-50

539 and allowed to recover prior to imaging or lethality analysis. Knockdown time for the following targets:

540 *baf-1* (48-72 hr), *emr-1* (24 hr), *lem-4* (24 hr), *chmp-7* (28 hr).

541

542 **Lethality and brood size quantification**

543 L4 worms were singled (uninjected) or injected with indicated dsRNA and allowed to recover for 24 hours

544 at 20°C. Worms were then singled to individual plates for 24 hours (day 1). Worms were transferred to

545 another plate for a final 24 hours (day 2). Worms were then killed and plates corresponding to 24-48 hours

546 post-injection (day 1) were counted for hatched larvae and unhatched embryos. The next day the plate

547 corresponding to 48-72 hours post-injection (day 2) were counted. The total number of embryos and larvae

548 were combined for each time window to calculate the brood size and the 48-72 hr embryonic lethality is

549 reported.

550

551 **Immunoblots**

552 *Generation of whole worm lysate*

553    Prior to lysate generation, L4 worms were selected 24 hours prior. For each sample, a microcentrifuge tube

554    was filled with 30 μl of M9 Buffer and volume was marked. 35 adult worms were singled on to an indented

555    slide filled with 75 ul of M9 + 0.1% Triton-X100. Worms were then collected into the marked

556    microcentrifuge tube and washed three times with M9 + 0.1% Triton X-100 (200 x g, 2 minutes). After the

557    final wash, samples were brought up to a final volume of 30 μl using M9 + 0.1% Triton. Then, 10 μl of 4X

558    Laemmli sample buffer was added and the tubes were mixed. The samples were then sonicated at 70°C for

559    15 minutes, followed by incubation for five minutes at 95°C. Samples were re-sonicated at 70°C for an

560    additional 15 minutes. Worm lysates were stored at -20°C until they were run on an SDS-PAGE protein

561    gel.

562

563    *Gel electrophoresis*

564    Worm lysates were loaded on a 4-20% Mini-Protean TGX Precast Gel (Bio-Rad). The gel was run at 120V

565    for 15 minutes to fully collapse samples and then 180V. Transfer to PDVF (Thermo Scientific) was

566    performed at 4°C at 350mA for 1.25 hr. Membranes were blocked in 5% non-fat milk/TBST for one hour

567    at room temperature and incubated overnight at 4°C with the following primary antibodies diluted in

568    blocking reagent: 1 μg/mL mouse α-alpha-tubulin (DM1A, EMD Millipore), 1 μg/mL rabbit α-LEM-2

569    (Novus Biologicals), 1 μg/mL rabbit α-CHMP-7 (Shankar et al., 2022) and rabbit α-BAF-1 (Gorjanacz et

570    al., 2007). The following day, membranes were briefly rinsed in TBS followed by three five-minute washes

571    in TBST. Membranes were then incubated with appropriate secondary antibodies for 1.25 hrs at room

572    temperature. Secondary antibodies were diluted 1:10,000 for horseradish peroxidase (HRP)-conjugated

573    goat-anti-rabbit and HRP-conjugated goat-anti-mouse (Thermo Fischer Scientific). Membranes were again

574    briefly rinsed in TBS followed by three five-minute washes in TBST. Membranes were incubated with

575    Clarity Max Western ECL Substrate (BIO-RAD) for five minutes before imaging (BioRad ChemiDoc MP

576    Imaging Systems).

577

578    **Immunofluorescence**

579    *Slide preparation*

580    Microscope slides (Fisher Scientific Premium Microscope Slides Superfrost) were coated with poly-L-

581    lysine (1 μg/mL) and dried on a heat-block. Slides were then baked at 95°C for 30 minutes and used the

582    same day.

583

584    *Fixation and immunofluorescence*

585    15-20 adult worms were picked into a 4 μl drop of ddH$_2$O and covered with a standard 18x18mm coverslip.

586    Embryos were pushed out of the adult worms by pressing down on the corners of the coverslip with a pipet

587      tip. To crack the eggshell and permeabilize the embryos, slides were placed in liquid nitrogen for ~five-

588      minutes. Coverslips were quickly removed by razor blade to pop off the coverslip. Slides were then fixed

589      in pre-chilled 100% methanol at -20 °C for 20 minutes. Following fixation, slides were washed two times

590      in 1X PBS at room temperature for 10 minutes each using a coplin jar. After the second wash, samples were

591      blocked with 1 % BSA in PBS per slide in a humid chamber for one hour at room temperature. Slides were

592      then incubated overnight at 4°C with primary antibodies diluted in PBS (45 μl per slide; rabbit α-LMN-1

593      (1 μg/mL) (Penfield et al., 2018). Following primary antibody incubation, slides were washed two times in

594      1X PBS+ 0.2%Tween 20 (PBST) at room temperature for 10 minutes each using a coplin jar. Following

595      the second wash, slides were incubated at room temperature for two hours in the dark with secondary

596      antibodies, anti-rabbit Cy3/Rhodamine, 1:200; anti-mouse FITC, 1:200 (Jackson Immunoresearch), diluted

597      in PBS. Slides were again washed two times in PBST at room temperature for 10 minutes each in the dark.

598      Samples were stained with 1 μg/mL Hoechst (diluted from a 1 mg/mL stock in $H_2O$) for 10 minutes. Slides

599      were washed quickly once with PBS at room temperature prior to mounting. Mounting media (Molecular

600      Probes ProLong Diamond Antifade Reagent) was added to each sample and coverslips were adhered with

601      clear nail-polish. Slides were dried at room temperature overnight and stored at –20°C.

602

603      **Microscopy**

604      *Live-cell imaging*

605      2% agarose imaging pads were made by sandwiching molten agarose (95°C) on a glass slide. Gravid adult

606      hermaphrodites were dissected using G10 beveled needles in 7 μl of Egg Salts (88.5 mM NaCl, 30mM KCl,

607      2.55 mM $MgCl_2$, 2.55 mM $CaCl_2$, 3.75 mM HEPES pH 7.4) on a glass slide. Select embryos were

608      transferred to the imaging pad using a mouth pipette. Stage of interest embryos were delicately positioned

609      using an eyelash tool and a glass coverslip was gently added on top of the imaging pad. Imaging was

610      performed on an inverted Nikon (Melville, NY) Ti microscope with a 60X (1.4 NA) Plan Apo objective

611      lens, a confocal scanner unit (CSU-XI, Yokogawa) with solid state 150-mW 488-nm and 100-mW 560-nm

612      lasers, and an ORCA R-3 Digital CCD Camera (Hamamatsu). For most experiments, images were acquired

613      every 20 seconds at five 2 μm-step z-slices. Imaging was performed in a temperature-controlled room at

614      20°C.

615

616      *Live-cell meiosis imaging*

617      Early embryo imaging, prior to eggshell formation, has been previously described (Maddox and Maddox,

618      2012). In brief, a circle of vasoline is drawn on a 24 x 50mm coverslip (Fisherbrand). 3 μl of Egg Salts are

619      added to the center of the circle to dissect embryos from gravid adults. A second long coverslip is placed

620    on top of first coverslip to form a droplet. Embryos are imaged in the suspended droplet with the vasoline

621    preventing any harmful compression.

622

623    *Fixed imaging*

624    Immunofluorescent, fixed embryo imaging was conducted on an inverted Nikon Ti2 Eclipse microscope

625    equipped with solid state 405, 445, 488, 515, 594, 561, 594, and 640 nm lasers, a Yokogawa CSU-W1

626    confocal scanner unit, a 60X (1.4 NA) Plan Apo objective lens, and a Prime BSI sCMOS camera

627    (Photometrics).

628

629    **Image analysis**

630    *Nuclear import analysis*

631    To determine the fluorescence intensity of NLS-LacI:GFP inside the nucleus of one-cell stage embryos, the

632    chromatin was traced with either the freehand or circle tool in ImageJ. Camera background was determined

633    by drawing a 50x50 pixel box in vacant areas of the time lapse. Average cytoplasmic values were

634    determined by drawing a 20x20 pixel box inside the embryo, away from the growing nucleus. The nuclear

635    to cytoplasmic ratio (N:C) was determined by subtracting the average camera background from each value

636    and then the nuclear value was divided by the cytoplasmic value. To account for differences in nuclear size,

637    the ratio was then multiplied by the nuclear area. The import of the NLS-LacI:GFP in to the pronuclei was

638    graphed relative to pseudocleavage regression.

639

640    *Line scan analysis of proteins at nuclear envelope and nucleoplasm*

641    A five-pixel wide line was drawn and across the entire nucleus to determine the fluorescence intensity. Line

642    scans (14 µm) along the maternal pronucleus were done at 200 seconds prior to pseudocleavage regression.

643    Lines were drawn to avoid internal membranes to gather isolated nucleoplasmic values. The same line scan

644    was used to acquire the average intensity for camera background and average was subtracted from all

645    values. These values were then plotted against the relative position along the line. The two maximum peaks

646    of the nuclear envelope values were averaged for the "nuclear envelope" value. ~15-25 values were

647    averaged in the nucleoplasm area to represent the nucleoplasmic value. The averaged nuclear envelope

648    value was divided by the nucleoplasmic value to calculate the nuclear envelope : nucleoplasmic ratio.

649

650    *Line scan analysis of nuclear envelope protein dynamics during meiosis and mitosis*

651    A three-pixel wide by five-micron long line was drawn on the reforming nuclear envelope. Anaphase II

652    onset was defined as the start of anaphase B with visible separation of chromatin away from the second

653    polar body at the cortex. Line scans of nascent membrane at anaphase onset were drawn along chromatin

654 mass using the line or free-hand tool in ImageJ. The same line scan was used to acquire the average intensity

655 for camera background and the average was subtracted from all values. These values were then plotted

656 against the relative position along the line. Line scans of sealing plaque/puncta enrichment were drawn

657 through the enrichment to the opposite nuclear membrane using the line tool. The maximum peak values

658 of the sealing plaque were divided by the values at the opposing nuclear rim to calculate the "LEM-2 puncta

659 accumulation". A similar technique was used to track sealing plaque proteins during mitosis. The free-hand

660 line tool was used to draw a three-pixel wide line over one face of nuclear membrane alongside chromatin

661 over time. These values were background-subtracted using an averaged camera background value. 5 values

662 at each end of the line, representing the "non-core" regions, were averaged. The maximum intensity values

663 along the line were divided by the non-core average to track core-domain enrichment over time (see Fig.

664 S3E).

665

666 **Statistical Analysis**

667 All statistical tests were performed using GraphPad Prism 9. Statistical analysis was performed on

668 datasets with multiple samples and from independent biological repeats. Statistical tests used, sample

669 sizes, definitions of replicates (N, n), and p values ($p < 0.05$ as significance cutoff) are reported in figures,

670 and/or figure legends, or text.

671

672

673

**References**

**Ahn, J.-H., Cho, M.-G., Sohn, S. and Lee, J.-H.** (2019). Inhibition of PP2A activity by H2O2 during mitosis disrupts nuclear envelope reassembly and alters nuclear shape. *Experimental & Molecular Medicine* **51**, 1–18.

**Asencio, C., Davidson, I. F., Santarella-Mellwig, R., Ly-Hartig, T. B., Mall, M., Wallenfang, M. R., Mattaj, I. W. and Gorjanacz, M.** (2012). Coordination of kinase and phosphatase activities by Lem4 enables nuclear envelope reassembly during mitosis. *Cell* **150**, 122–35.

**Audhya, A., Desai, A. and Oegema, K.** (2007). A role for Rab5 in structuring the endoplasmic reticulum. *J Cell Biol* **178**, 43–56.

**Bahmanyar, S., Biggs, R., Schuh, A. L., Desai, A., Müller-Reichert, T., Audhya, A., Dixon, J. E. and Oegema, K.** (2014). Spatial control of phospholipid flux restricts endoplasmic reticulum sheet formation to allow nuclear envelope breakdown. *Genes Dev* **28**, 121–126.

**Barger, S. R., Penfield, L. and Bahmanyar, S.** (2022). Coupling lipid synthesis with nuclear envelope remodeling. *Trends in Biochemical Sciences* **47**, 52–65.

**Barkan, R., Zahand, A. J., Sharabi, K., Lamm, A. T., Feinstein, N., Haithcock, E., Wilson, K. L., Liu, J. and Gruenbaum, Y.** (2012). Ce-emerin and LEM-2: essential roles in Caenorhabditis elegans development, muscle function, and mitosis. *Mol Biol Cell* **23**, 543–552.

**Barton, L. J., Soshnev, A. A. and Geyer, P. K.** (2015). Networking in the nucleus: a spotlight on LEM-domain proteins. *Curr Opin Cell Biol* **34**, 1–8.

**Bauer, I., Brune, T., Preiss, R. and Kölling, R.** (2015). Evidence for a Nonendosomal Function of the Saccharomyces cerevisiae ESCRT-III-Like Protein Chm7. *Genetics* **201**, 1439–1452.

**Bone, C. R., Tapley, E. C., Gorjánácz, M. and Starr, D. A.** (2014). The Caenorhabditis elegans SUN protein UNC-84 interacts with lamin to transfer forces from the cytoplasm to the nucleoskeleton during nuclear migration. *Mol Biol Cell* **25**, 2853–2865.

**Cai, M., Huang, Y., Suh, J. Y., Louis, J. M., Ghirlando, R., Craigie, R. and Clore, G. M.** (2007). Solution NMR structure of the barrier-to-autointegration factor-Emerin complex. *J Biol Chem* **282**, 14525–35.

**Coyne, A. N., Baskerville, V., Zaepfel, B. L., Dickson, D. W., Rigo, F., Bennett, F., Lusk, C. P. and Rothstein, J. D.** (2021). Nuclear accumulation of CHMP7 initiates nuclear pore complex injury and subsequent TDP-43 dysfunction in sporadic and familial ALS. *Sci Transl Med* **13**,604(2021): eabe1923.

**Davis, P., Zarowiecki, M., Arnaboldi, V., Becerra, A., Cain, S., Chan, J., Chen, W. J., Cho, J., da Veiga Beltrame, E., Diamantakis, S., et al.** (2022). WormBase in 2022-data, processes, and tools for analyzing Caenorhabditis elegans. *Genetics* **220**, iyac003.

**Dickinson, D. J. and Goldstein, B.** (2016). CRISPR-Based Methods for Caenorhabditis elegans Genome Engineering. *Genetics* **202**, 885–901.

711 **Dittrich, C. M., Kratz, K., Sendoel, A., Gruenbaum, Y., Jiricny, J. and Hengartner, M. O.** (2012).
712      LEM-3 - A LEM domain containing nuclease involved in the DNA damage response in C.
713      elegans. *PLoS One* **7**, e24555.

714 **Fabritius, A. S., Ellefson, M. L. and McNally, F. J.** (2011). Nuclear and spindle positioning during
715      oocyte meiosis. *Curr Opin Cell Biol* **23**, 78–84.

716 **Frøkjaer-Jensen, C., Davis, M. W., Hopkins, C. E., Newman, B. J., Thummel, J. M., Olesen, S.-P.,**
717      **Grunnet, M. and Jorgensen, E. M.** (2008). Single-copy insertion of transgenes in
718      Caenorhabditis elegans. *Nat Genet* **40**, 1375–1383.

719 **Gatta, A. T., Olmos, Y., Stoten, C. L., Chen, Q., Rosenthal, P. B. and Carlton, J. G.** (2021). CDK1
720      controls CHMP7-dependent nuclear envelope reformation. *Elife* **10**: e59999.

721 **Gauthier, B. R. and Comaills, V.** (2021). Nuclear Envelope Integrity in Health and Disease:
722      Consequences on Genome Instability and Inflammation. *Int J Mol Sci* **22**, 7281.

723 **Goddard, T. D., Huang, C. C., Meng, E. C., Pettersen, E. F., Couch, G. S., Morris, J. H. and Ferrin,**
724      **T. E.** (2018). UCSF ChimeraX: Meeting modern challenges in visualization and analysis: UCSF
725      ChimeraX Visualization System. *Protein Science* **27**, 14–25.

726 **González-Aguilera, C., Ikegami, K., Ayuso, C., de Luis, A., Íñiguez, M., Cabello, J., Lieb, J. D. and**
727      **Askjaer, P.** (2014). Genome-wide analysis links emerin to neuromuscular junction activity in
728      Caenorhabditis elegans. *Genome Biol* **15**, R21.

729 **Gorjanacz, M., Klerkx, E. P., Galy, V., Santarella, R., Lopez-Iglesias, C., Askjaer, P. and Mattaj, I.**
730      **W.** (2007). Caenorhabditis elegans BAF-1 and its kinase VRK-1 participate directly in post-
731      mitotic nuclear envelope assembly. *EMBO J* **26**, 132–43.

732 **Gu, M., LaJoie, D., Chen, O. S., von Appen, A., Ladinsky, M. S., Redd, M. J., Nikolova, L.,**
733      **Bjorkman, P. J., Sundquist, W. I., Ullman, K. S., et al.** (2017). LEM2 recruits CHMP7 for
734      ESCRT-mediated nuclear envelope closure in fission yeast and human cells. *Proc Natl Acad Sci*
735      *U S A* **114**, E2166–E2175.

736 **Halfmann, C. T., Sears, R. M., Katiyar, A., Busselman, B. W., Aman, L. K., Zhang, Q., O'Bryan, C.**
737      **S., Angelini, T. E., Lele, T. P. and Roux, K. J.** (2019). Repair of nuclear ruptures requires
738      barrier-to-autointegration factor. *J Cell Biol* **218**, 2136–2149.

739 **Haraguchi, T., Koujin, T., Osakada, H., Kojidani, T., Mori, C., Masuda, H. and Hiraoka, Y.** (2007).
740      Nuclear localization of barrier-to-autointegration factor is correlated with progression of S phase
741      in human cells. *J Cell Sci* **120**, 1967–1977.

742 **Haraguchi, T., Kojidani, T., Koujin, T., Shimi, T., Osakada, H., Mori, C., Yamamoto, A. and**
743      **Hiraoka, Y.** (2008). Live cell imaging and electron microscopy reveal dynamic processes of
744      BAF-directed nuclear envelope assembly. *J Cell Sci* **121**, 2540–54.

745 **Harr, J. C., Schmid, C. D., Muñoz-Jiménez, C., Romero-Bueno, R., Kalck, V., Gonzalez-Sandoval,**
746      **A., Hauer, M. H., Padeken, J., Askjaer, P., Mattout, A., et al.** (2020). Loss of an H3K9me
747      anchor rescues laminopathy-linked changes in nuclear organization and muscle function in an
748      Emery-Dreifuss muscular dystrophy model. *Genes Dev* **34**, 560–579.

24

749 **Hastie, E., Sellers, R., Valan, B. and Sherwood, D. R.** (2019). A Scalable CURE Using a CRISPR/Cas9
750       Fluorescent Protein Knock-In Strategy in Caenorhabditis elegans. *J Microbiol Biol Educ* **20**,
751       20.3.60.

752 **Hayashi, H., Kimura, K. and Kimura, A.** (2012). Localized accumulation of tubulin during semi-open
753       mitosis in the Caenorhabditis elegans embryo. *Mol Biol Cell* **23**, 1688–1699.

754 **Holaska, J. M., Lee, K. K., Kowalski, A. K. and Wilson, K. L.** (2003). Transcriptional repressor germ
755       cell-less (GCL) and barrier to autointegration factor (BAF) compete for binding to emerin in
756       vitro. *J Biol Chem* **278**, 6969–6975.

757 **Jumper, J., Evans, R., Pritzel, A., Green, T., Figurnov, M., Ronneberger, O., Tunyasuvunakool, K.,
758       Bates, R., Žídek, A., Potapenko, A., et al.** (2021). Highly accurate protein structure prediction
759       with AlphaFold. *Nature* **596**, 583–589.

760 **Kono, Y., Adam, S. A., Sato, Y., Reddy, K. L., Zheng, Y., Medalia, O., Goldman, R. D., Kimura, H.
761       and Shimi, T.** (2022). Nucleoplasmic lamin C rapidly accumulates at sites of nuclear envelope
762       rupture with BAF and cGAS. *J Cell Biol* **221**(12): e202201024.

763 **Lee, K. K., Gruenbaum, Y., Spann, P., Liu, J. and Wilson, K. L.** (2000). C. elegans nuclear envelope
764       proteins emerin, MAN1, lamin, and nucleoporins reveal unique timing of nuclear envelope
765       breakdown during mitosis. *Mol Biol Cell* **11**, 3089–3099.

766 **Lin, F., Blake, D. L., Callebaut, I., Skerjanc, I. S., Holmer, L., McBurney, M. W., Paulin-Levasseur,
767       M. and Worman, H. J.** (2000). MAN1, an inner nuclear membrane protein that shares the LEM
768       domain with lamina-associated polypeptide 2 and emerin. *J Biol Chem* **275**, 4840–4847.

769 **Liu, S. and Pellman, D.** (2020). The coordination of nuclear envelope assembly and chromosome
770       segregation in metazoans. *Nucleus* **11**, 35–52.

771 **Liu, J., Lee, K. K., Segura-Totten, M., Neufeld, E., Wilson, K. L. and Gruenbaum, Y.** (2003). MAN1
772       and emerin have overlapping function(s) essential for chromosome segregation and cell division
773       in Caenorhabditis elegans. *Proc Natl Acad Sci U S A* **100**, 4598–603.

774 **Maddox, A. S. and Maddox, P. S.** (2012). High-resolution imaging of cellular processes in
775       Caenorhabditis elegans. *Methods Cell Biol* **107**, 1–34.

776 **Marcelot, A., Petitalot, A., Ropars, V., Le Du, M. H., Samson, C., Dubois, S., Hoffmann, G., Miron,
777       S., Cuniasse, P., Marquez, J. A., et al.** (2021). Di-phosphorylated BAF shows altered structural
778       dynamics and binding to DNA, but interacts with its nuclear envelope partners. *Nucleic Acids Res*
779       **49**, 3841–3855.

780 **Margalit, A., Segura-Totten, M., Gruenbaum, Y. and Wilson, K. L.** (2005). Barrier-to-autointegration
781       factor is required to segregate and enclose chromosomes within the nuclear envelope and
782       assemble the nuclear lamina. *Proc Natl Acad Sci U S A* **102**, 3290–5.

783 **Mirdita, M., Schütze, K., Moriwaki, Y., Heo, L., Ovchinnikov, S. and Steinegger, M.** (2022).
784       ColabFold: making protein folding accessible to all. *Nat Methods* **19**, 679–682

785 **Morales-Martínez, A., Dobrzynska, A. and Askjaer, P.** (2015). Inner nuclear membrane protein LEM-
786     2 is required for correct nuclear separation and morphology in C. elegans. *J Cell Sci* **128**, 1090–
787     1096.

788 **Nicholas R. Ader, Linda Chen, Ivan V. Surovtsev, William L. Chadwick, Megan C. King, and C.**
789     **Patrick Lusk** (2022). An ESCRT grommet cooperates with a diffusion barrier to maintain
790     nuclear integrity. *bioRxiv* 2022.12.12.520126.

791 **Oegema, K and Hyman, A.A.** (2006). Cell division. *WormBook*. 19:1–40.

792 **Olmos, Y., Perdrix-Rosell, A. and Carlton, J. G.** (2016). Membrane Binding by CHMP7 Coordinates
793     ESCRT-III-Dependent Nuclear Envelope Reformation. *Curr Biol* **26**, 2635–2641.

794 **Paix, A., Folkmann, A., Rasoloson, D. and Seydoux, G.** (2015). High Efficiency, Homology-Directed
795     Genome Editing in Caenorhabditis elegans Using CRISPR-Cas9 Ribonucleoprotein Complexes.
796     *Genetics* **201**, 47–54.

797 **Penfield, L., Wysolmerski, B., Mauro, M., Farhadifar, R., Martinez, M. A., Biggs, R., Wu, H.-Y.,**
798     **Broberg, C., Needleman, D. and Bahmanyar, S.** (2018). Dynein pulling forces counteract
799     lamin-mediated nuclear stability during nuclear envelope repair. *Mol Biol Cell* **29**, 852–868.

800 **Penfield, L., Shankar, R., Szentgyörgyi, E., Laffitte, A., Mauro, M. S., Audhya, A., Müller-Reichert,**
801     **T. and Bahmanyar, S.** (2020). Regulated lipid synthesis and LEM2/CHMP7 jointly control
802     nuclear envelope closure. *J Cell Biol* **219**, e201908179.

803 **Pettersen, E. F., Goddard, T. D., Huang, C. C., Meng, E. C., Couch, G. S., Croll, T. I., Morris, J. H.**
804     **and Ferrin, T. E.** (2021). UCSF CHIMERAX : Structure visualization for researchers, educators,
805     and developers. *Protein Science* **30**, 70–82.

806 **Rodriguez-Muñoz, M., Anglada, T. and Genescà, A.** (2022). A matter of wrapper: Defects in the
807     nuclear envelope of lagging and bridging chromatin threatens genome integrity. *Seminars in Cell*
808     *& Developmental Biology* **123**, 124–130.

809 **Samson, C., Petitalot, A., Celli, F., Herrada, I., Ropars, V., Le Du, M.-H., Nhiri, N., Jacquet, E.,**
810     **Arteni, A.-A., Buendia, B., et al.** (2018). Structural analysis of the ternary complex between
811     lamin A/C, BAF and emerin identifies an interface disrupted in autosomal recessive progeroid
812     diseases. *Nucleic Acids Research* **46**, 10460–10473.

813 **Samwer, M., Schneider, M. W. G., Hoefler, R., Schmalhorst, P. S., Jude, J. G., Zuber, J. and**
814     **Gerlich, D. W.** (2017). DNA Cross-Bridging Shapes a Single Nucleus from a Set of Mitotic
815     Chromosomes. *Cell* **170**, 956-972.e23.

816 **Sears, R. M. and Roux, K. J.** (2020). Diverse cellular functions of barrier-to-autointegration factor and
817     its roles in disease. *Journal of Cell Science* **133**, jcs246546.

818 **Shankar, R., Lettman, M. M., Whisler, W., Frankel, E. B. and Audhya, A.** (2022). The ESCRT
819     machinery directs quality control over inner nuclear membrane architecture. *Cell Rep* **38**, 110263.

820 **Snyers, L., Erhart, R., Laffer, S., Pusch, O., Weipoltshammer, K. and Schöfer, C.** (2018).
821     LEM4/ANKLE-2 deficiency impairs post-mitotic re-localization of BAF, LAP2α and LaminA to

822     the nucleus, causes nuclear envelope instability in telophase and leads to hyperploidy in HeLa
823     cells. *Eur J Cell Biol* **97**, 63–74.

824     **Thaller, D. J., Allegretti, M., Borah, S., Ronchi, P., Beck, M. and Lusk, C. P.** (2019). An ESCRT-
825     LEM protein surveillance system is poised to directly monitor the nuclear envelope and nuclear
826     transport system. *Elife* **8**, e45284.

827     **Thaller, D. J., Tong, D., Marklew, C. J., Ader, N. R., Mannino, P. J., Borah, S., King, M. C., Ciani,**
828     **B. and Lusk, C. P.** (2021). Direct binding of ESCRT protein Chm7 to phosphatidic acid-rich
829     membranes at nuclear envelope herniations. *J Cell Biol* **220**,.

830     **Ungricht, R. and Kutay, U.** (2017). Mechanisms and functions of nuclear envelope remodelling. *Nature*
831     *Reviews Molecular Cell Biology* **18**, 229–245.

832     **Varadi, M., Anyango, S., Deshpande, M., Nair, S., Natassia, C., Yordanova, G., Yuan, D., Stroe, O.,**
833     **Wood, G., Laydon, A., et al.** (2022). AlphaFold Protein Structure Database: massively
834     expanding the structural coverage of protein-sequence space with high-accuracy models. *Nucleic*
835     *Acids Res* **50**, D439–D444.

836     **Ventimiglia, L. N., Cuesta-Geijo, M. A., Martinelli, N., Caballe, A., Macheboeuf, P., Miguet, N.,**
837     **Parnham, I. M., Olmos, Y., Carlton, J. G., Weissenhorn, W., et al.** (2018). CC2D1B
838     Coordinates ESCRT-III Activity during the Mitotic Reformation of the Nuclear Envelope. *Dev*
839     *Cell* **47**, 547-563.e6.

840     **Vietri, M., Schink, K. O., Campsteijn, C., Wegner, C. S., Schultz, S. W., Christ, L., Thoresen, S. B.,**
841     **Brech, A., Raiborg, C. and Stenmark, H.** (2015). Spastin and ESCRT-III coordinate mitotic
842     spindle disassembly and nuclear envelope sealing. *Nature* **522**, 231–5.

843     **Vietri, M., Schultz, S. W., Bellanger, A., Jones, C. M., Petersen, L. I., Raiborg, C., Skarpen, E.,**
844     **Pedurupillay, C. R. J., Kjos, I., Kip, E., et al.** (2020). Unrestrained ESCRT-III drives
845     micronuclear catastrophe and chromosome fragmentation. *Nat Cell Biol* **22**, 856–867.

846     **von Appen, A., LaJoie, D., Johnson, I. E., Trnka, M. J., Pick, S. M., Burlingame, A. L., Ullman, K.**
847     **S. and Frost, A.** (2020). LEM2 phase separation promotes ESCRT-mediated nuclear envelope
848     reformation. *Nature* **582**, 115–118.

849     **Young, A. M., Gunn, A. L. and Hatch, E. M.** (2020). BAF facilitates interphase nuclear membrane
850     repair through recruitment of nuclear transmembrane proteins. *Mol Biol Cell* **31**, 1551–1560.

851     **Zheng, R., Ghirlando, R., Lee, M. S., Mizuuchi, K., Krause, M. and Craigie, R.** (2000). Barrier-to-
852     autointegration factor (BAF) bridges DNA in a discrete, higher-order nucleoprotein complex.
853     *Proc Natl Acad Sci U S A* **97**, 8997–9002.

854

855

856

857

858 **Figures**

**Barger et al. Figure 1**



859
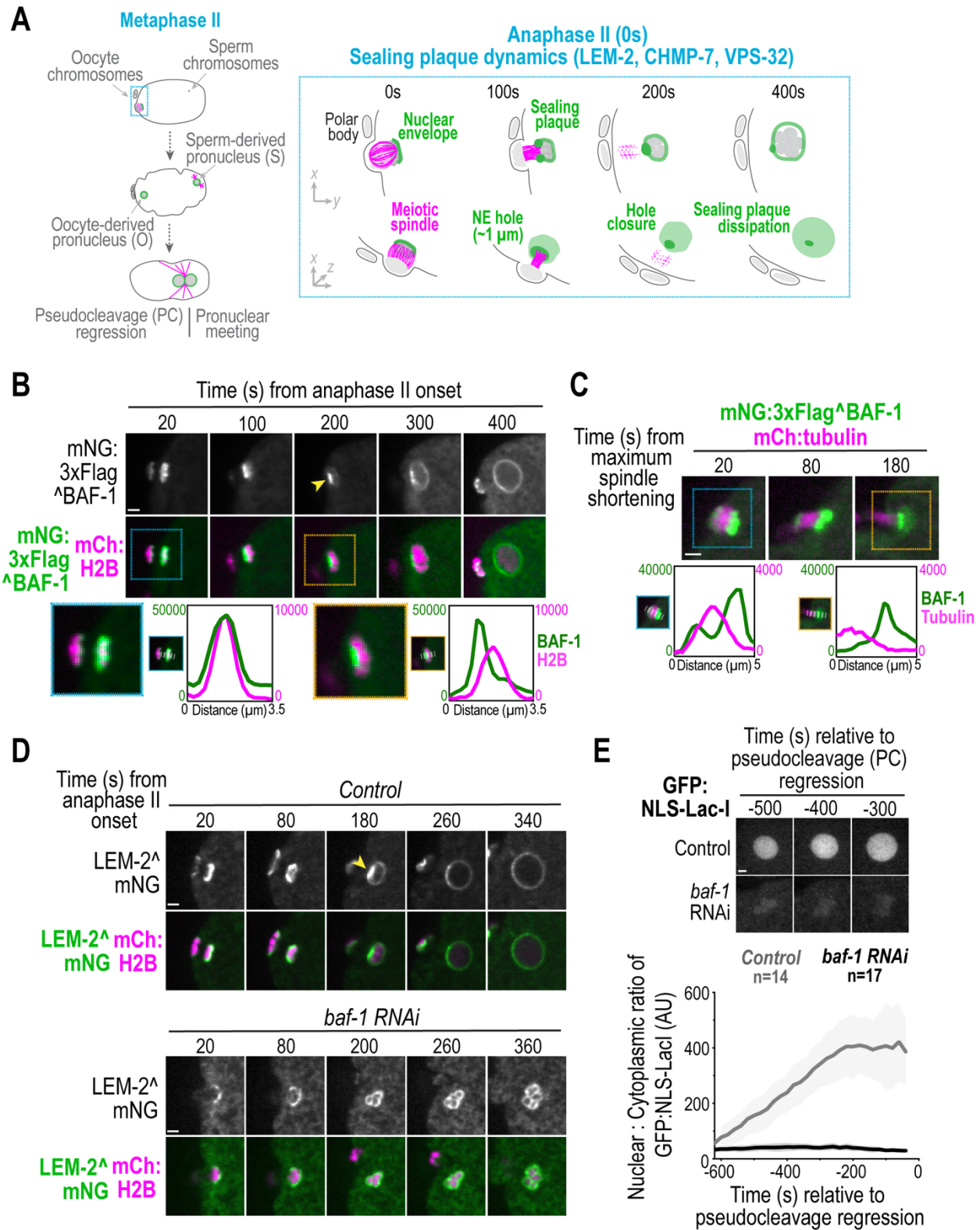
860 **Figure 1. BAF-1 is required for sealing plaque formation during meiosis II in *C. elegans*** (A) Left,

861 Schematic representation of oocyte- and sperm-derived pronuclear formation and migration after meiosis

862 II. Right (box), schematic of sealing plaque dynamics relative to anaphase II. (B) Spinning disk confocal

863 images from time lapse series of mNG^BAF-1 dynamics relative to anaphase II. Yellow arrowhead marks

864 sealing plaque. Below, zoom insets of select frames for background-corrected line scans of indicated

865 markers at indicated timepoints. Time in seconds relative to anaphase II onset. (C) Spinning disk confocal

866 images from time lapse series of mNG^BAF-1 (green) and meiotic spindle microtubules (magenta).

867 Below, zoom insets of select frames for background-corrected line scans of indicated markers at indicated

868 timepoints.  Time in seconds relative to maximum spindle shortening. (D) Spinning disk confocal images

869 from time lapse series of LEM-2^mNG in indicated conditions. Yellow arrowhead marks sealing plaque.

870 Time in seconds relative to anaphase onset. (E) Above, Spinning disk confocal images of GFP:NLS:LacI

871 fluorescence in oocyte-derived pronucleus in indicated conditions. Below, plot (average ± SD) of

872 normalized nuclear GFP:NLS-LacI fluorescence for indicated conditions. Time in seconds relative to

873 pseudocleavage (PC) regression. n = # of embryos. Scale bars, 2 μm.
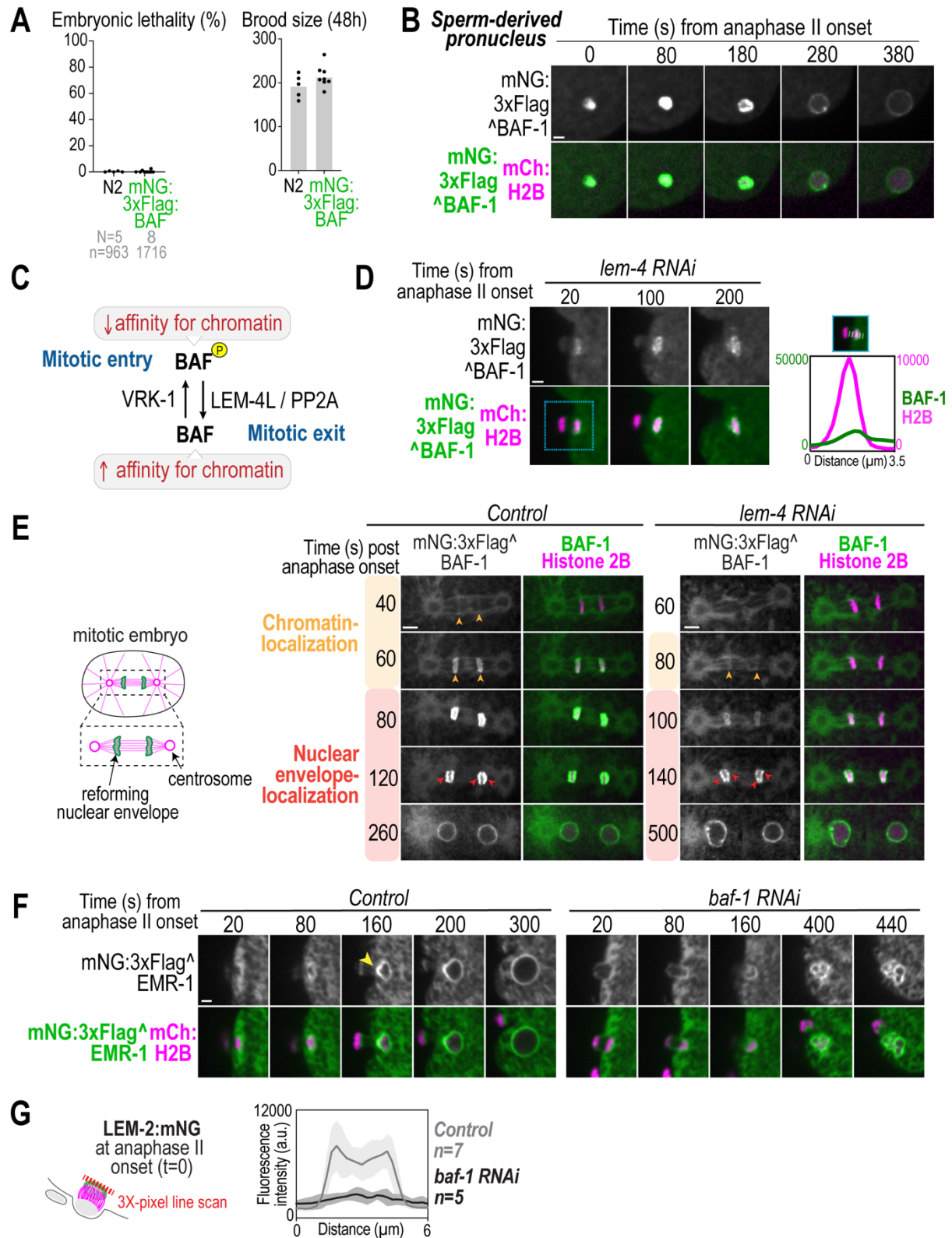
875    **Figure S1. Regulation of BAF-1 dynamics**, related to Figure 1. (A) Plot representing percentage of

876    embryonic lethality and brood size in indicated conditions. N = # of worms, n = # of embryos. (B)

877    Spinning disk confocal images from time lapse series of endogenous mNG^BAF-1 localization on sperm-

878    derived pronucleus. Time in seconds relative to anaphase II onset. (C) Schematic of phosphoregulation of

879    BAF-1 and the effect on chromatin interaction. (D) Left, spinning disk confocal time lapse images of

880    mNG^BAF-1 and mCh:Histone(H)2B with *lem-4* RNAi in oocyte meiosis II. Time is in seconds relative

881    to anaphase II. Right, plot of background-corrected line scan of indicated markers. (E) Left, schematic

882    representation of reforming nuclear envelopes after first mitotic division in *C. elegans*. Right, spinning

883    disk confocal time lapse series of mNG^BAF-1 and mCh:Histone(H)2B in indicated conditions. Color of

884    arrowheads correspond to colored labels. Time in seconds relative to mitotic anaphase onset. Scale bar, 5

885    μm. (F) Spinning disk confocal images from time lapse series of mNG^EMR-1 dynamics during oocyte-

886    derived pronuclear formation in indicated conditions. Yellow arrow marks sealing plaque. Time in

887    seconds relative to anaphase II onset. Scale bar, 2 μm. (G) Left, schematic of (Right) line scan analysis

888    (average ± SD) of LEM-2^mNG at nuclear rim at anaphase II onset in indicated conditions. n = # of

889    embryos.

890
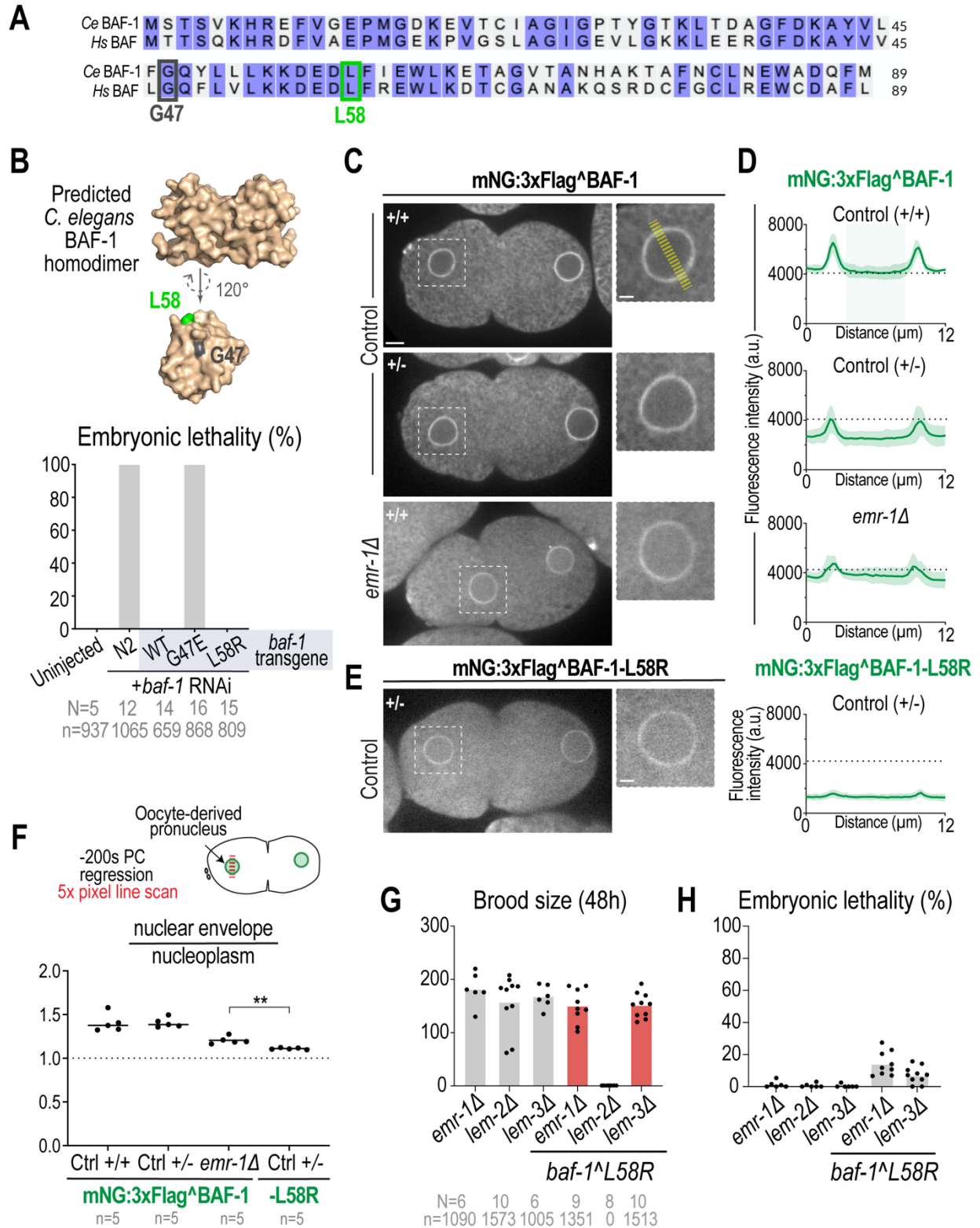
891    **Figure 2. A mutation in BAF-1 that selectively inhibits LEM-domain binding is non-essential in *C.***

892    ***elegans.*** (A) Amino acid sequence alignment of human BAF and *C. elegans* BAF-1. Identical amino acid

893    residues shaded in purple; mutations in indicated amino acid residues are boxed. (B) Above, 3D space

894    filling model of predicted *C. elegans* BAF-1 homodimer generated using (Miradita et al., 2022; Goddart

895    et al., 2018; Pettersen et al., 2021) and monomer using AlphaFold Protein Structure Database (Jumper et

896    al., 2021; Varadi et al., 2022). Monomer rotated 120 degrees on the x-axis relative to dimer with amino

897    acid residues mutated in this study highlighted. Below, Plot of percentage of embryonic lethality in

898    indicated conditions. N = # of worms, n = # of embryos. (C-E) Left, Spinning disk confocal images of

899    mNG^BAF-1 at 200 sec prior to pseudocleavage (PC) regression in indicated conditions. Homozygous

900    (+/+) or heterozygous (+/-) insertion of mNG at endogenous *baf-1* locus marked in images. Right, Plots of

901    background-corrected line scan (average ± SD) of mNG^BAF-1 (n = 5 embryos). Fluorescence signal

902    from nucleoplasm shaded in green in control. Scale bars, 5 μm; Scale bar in zoom insets, 2 μm. (F)

903    Above, Schematic representation of line scan analysis. Below, Plot representing ratio of mNG signal at

904    nuclear envelope (average of peak signals) and nucleoplasm (average signal between peaks) from line

905    scan analysis in indicated conditions. Statistical significance determined by Mann-Whitney test (**=p-

906    0.0079). n = # of embryos. (G, H) Plot representing embryonic lethality (G) and brood size (H) in

907    indicated conditions. N = # of worms, n = # of embryos.

**A** *C. elegans* BAF-1 re-encoded transgene: (Chr I, Mos)

baf-1 RNAi resistant

ATGTCGACTTCTGTTAAGCACCGTGAATTCGTGGGCGAAC-
CAATGGGGGATAAGGAGGTAGTGTATCGCAGGAATCGGGCC
AACGTATGGAACTAAATTGACCGACGCGGGCTTTGATAAAG-
TATGTAGATTTTTTTTTCTCAAATTTTCGATCAATGTTAAAA
TTTGAATTTCAGGCCTACGTCTTGTTCGGACAGTATCTCCT-
GCTTAAAAAGGATGAGGATCTGTTCATCGAGTGGCTGAAGG
AGACCGCGGGCGTCACAGCAAACCATGCTAAAACAGCAT-
TCAATTGCCTCAATGAGTGGGCCGACCAGTTCATGTAA

**B** Generation of *baf-1^L58R* by repair template:

*baf-1* (B0464.7) — 5' UTR — 1 — 2 — 3' UTR

Leu

Wild type    TGAAG**AAA**GACGAG**GATTTG**TTTATCG
*baf-1^L58R*  TGAAG**AAG**GACGAG**GACCGG**TTTATCG
                                    Arg

**C**

MW,kDa — N2 — *baf-1^ L58R* — *baf-1* RNAi (72h)
α-BAF serum
α-tubulin

**D** Embryonic lethality (%)    Brood size (48h)

N2  *baf-1^ L58R*        N2  *baf-1^ L58R*
N=10   11
n=2345  2049

**E** *baf-1* (B0464.7) > **mNG:3xFlag^BAF-1** (CRISPR-Cas9 gene editing of *baf-1* locus using pDD268 repair plasmid)

5' UTR — 1 — 2 — 3' UTR
ACAAAGAAGTCACATGCATCGC**CGG**GA
sgRNA                    PAM

5' UTR — mNG — 1 — 2 — 3' UTR
3xFLAG-AGACTAGGA-**ATG**

**F** *C. elegans* LEM-2

LEM domain | Transmembrane domain | Winged-helix / MSC domain

3 42                    400
1                        500

*Correctly annotated lem-2 (tm1582) protein product* | (region deletion and in-frame single base pair insertion)
(deletion of aa 23-283) | WormBase WS287

*Misannotated lem-2 (tm1582) protein product* | (single base pair insertion missing from annotation)
truncated protein (53 aa) | WormBase WS286

**G** Generation of *lem-2Δ* by NHEJ:

*lem-2* (W01G7.5)

5' UTR — 1 — 2 — 3 — 3' UTR

ca**GGT**accaccacaagtagggcgtggcgga        cgat**GGC**tacaagaacacgaaggcagacctttt
PAM      sgRNA                              PAM         sgRNA

**H**

N2  *lem-2Δ*
50 kDa —  α-LEM-2
50 kDa —  α-tubulin

**I** N2

*lem-2Δ; baf-1^L58R*

908

34

909     **Figure S2. Generation and analysis of *baf-1* and *lem-2* mutant alleles.** (A) Schematic showing single

910     copy insertion of the RNAi-resistant *baf-1* transgene integrated in the MosI transposon site of

911     chromosome I. (B) Schematic of CRISPR-Cas9 edits at endogenous *baf-1* locus to generate the *baf-*

912     *1(L58R)* mutant allele. (C) Representative immunoblot of whole worm lysates incubated with antibodies

913     against BAF in indicated conditions. N = 3 independent experiments. (D) Plots (average + replicates)

914     representing embryonic lethality and brood size in indicated conditions. N = # of worms, n = # of

915     embryos. (E) Schematic representation of endogenous *baf-1* locus with CRISPR guides used to insert

916     mNG. (F) Schematic representation of LEM-2 protein domain structure. Gray box, LEM-2 mutant protein

917     produced from correctly annotated *tm1582* mutant allele. Red box, LEM-2 mutant protein predicted from

918     misannotated *tm1582* mutant allele. (G) Schematic representation of endogenous *lem-2* locus and

919     CRISPR guides to excise the *lem-2* gene to generate the null allele used in this study. (H) Immunoblot of

920     whole worm lysates incubated with antibodies made against N-terminus (aa 1-100) of LEM-2 protein

921     (Novus Biologicals) in indicated strains. (I) Representative brightfield image of whole worms in indicated

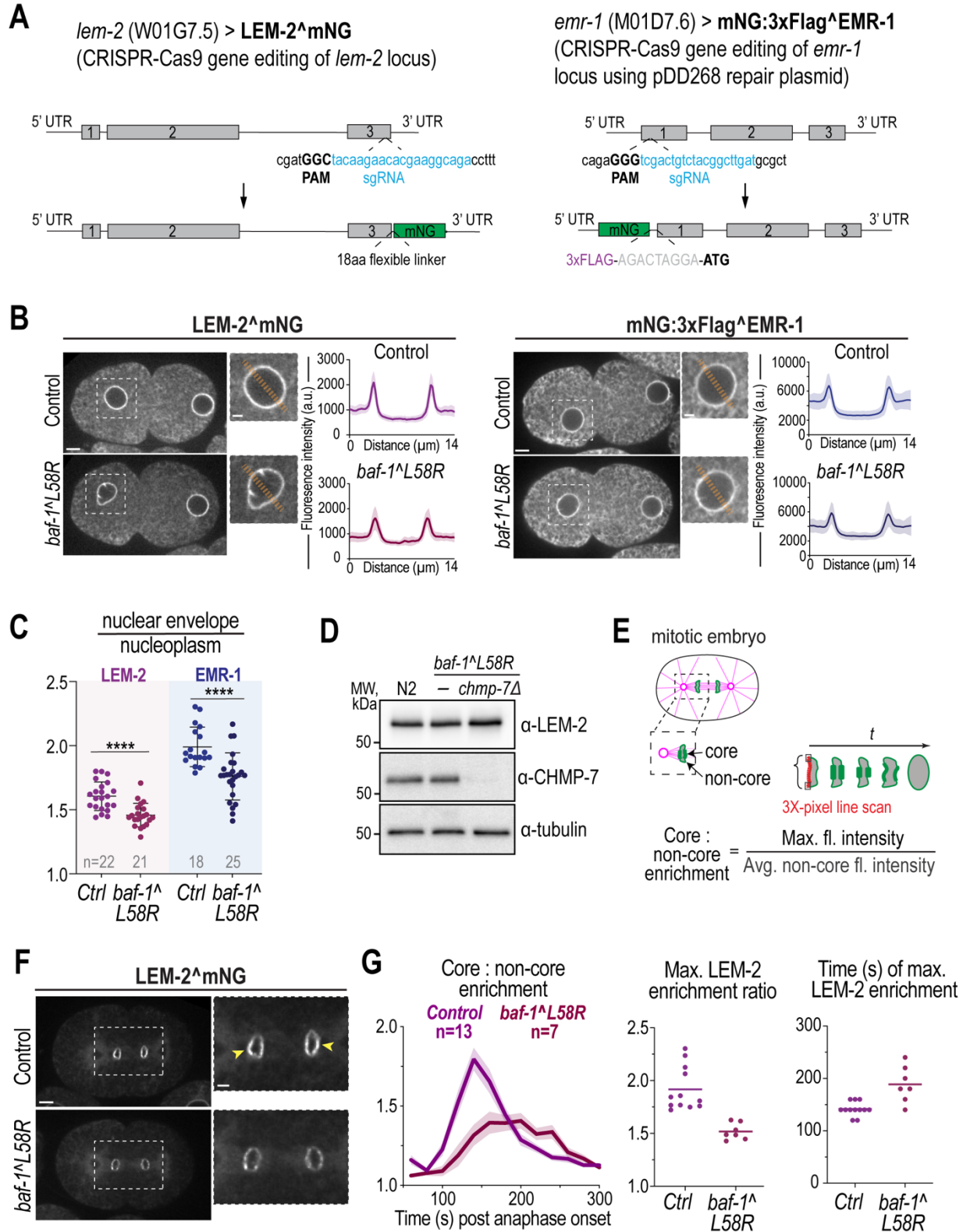922     strain. Black arrow points to germline/embryos. Scale bar, 50 μm.

**Barger et al. Figure 3**
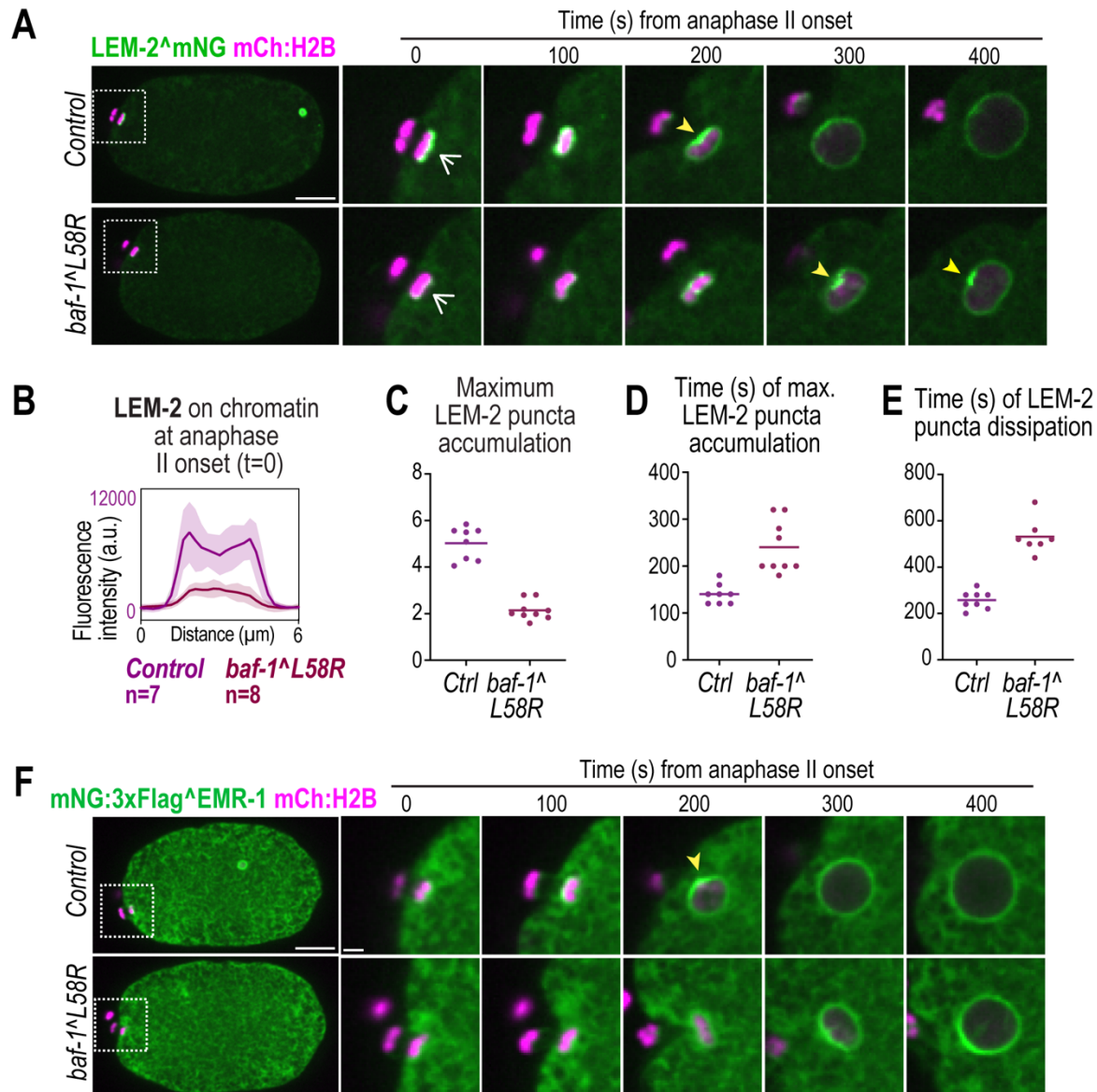


**Figure 3. BAF-LEM interactions orchestrate organized and timely recruitment of sealing proteins during nuclear envelope formation.** (A) Spinning disk confocal images from time lapse series of LEM-2^mNG during oocyte pronuclear formation in indicated conditions. (B) Plot of background-corrected line scan analysis (average ± SD) of LEM-2^mNG on at nuclear rim at anaphase II onset (white arrows at t = 0s) in indicated conditions. n = # of embryos. (C-D) Plots (average + replicates) representing maximum LEM-2 fluorescence signal at nuclear rim from time series in (C), time in seconds relative to anaphase onset II of maximum LEM-2^mNG fluorescence signal in (C) shown in (D), and time in seconds relative to anaphase onset II of LEM-2^mNG puncta dissipation shown in (E). (F) Spinning disk confocal images from time lapse series of mNG^EMR-1 in indicated conditions. Yellow arrows point to enrichment sites. Scale bars of whole embryo image, 10 μm, zoom insets scale bar, 2 μm.

36

**A**

*lem-2* (W01G7.5) > **LEM-2^mNG**
(CRISPR-Cas9 gene editing of *lem-2* locus)

*emr-1* (M01D7.6) > **mNG:3xFlag^EMR-1**
(CRISPR-Cas9 gene editing of *emr-1*
locus using pDD268 repair plasmid)

cgat**GGC**tacaagaacacgaaggcagaccttt
**PAM** sgRNA

caga**GGG**tcgactgtctacggcttgatgcgct
**PAM** sgRNA

18aa flexible linker

3xFLAG-AGACTAGGA-**ATG**

**B**



LEM-2^mNG

mNG:3xFlag^EMR-1

**C**



nuclear envelope / nucleoplasm

LEM-2    EMR-1

n=22    21    18    25

Ctrl    baf-1^L58R    Ctrl    baf-1^L58R

**D**



baf-1^L58R

MW, kDa    N2    −    chmp-7Δ

α-LEM-2

α-CHMP-7

α-tubulin

**E**

mitotic embryo

core
non-core

*t*

3X-pixel line scan

$$\text{Core : non-core enrichment} = \frac{\text{Max. fl. intensity}}{\text{Avg. non-core fl. intensity}}$$

**F**



LEM-2^mNG

Control

baf-1^L58R

**G**



Core : non-core enrichment
*Control* n=13    *baf-1^L58R* n=7

Time (s) post anaphase onset

Max. LEM-2 enrichment ratio

Ctrl    baf-1^L58R

Time (s) of max. LEM-2 enrichment

Ctrl    baf-1^L58R

934

37

935 **Figure S3. Generation of endogenous mNG tagged strains and analysis of dynamics and protein**

936 **levels of EMR-1 and LEM-2 in *baf-1(L58R)* mutant strain**, related to Figure 3 (A) Schematic

937 representations of endogenous gene loci of *emr-1* and *lem-1* with CRISPR guides used to insert mNG-tag.

938 (B) Left, representative confocal images of LEM-2^mNG and mNG^EMR-1 at oocyte- and sperm-

939 derived pronuclei at 200 sec prior to pseudocleavage (PC) regression. Right, line scan analysis (average +

940 SD) of LEM-2^mNG and mNG^EMR-1 at oocyte pronucleus at -200 sec releative to PC regression. n = #

941 of embryos. (C) Plot represents average ± SD + replicates of NE:nucleoplasmic ratios of indicated

942 proteins at oocyte pronucleus in indicated conditions. Statistical significance determined by unpaired

943 Student's t-test (****=$p<0.0001$). n = # of embryos. (D) Representative immunoblot of whole worm

944 lysates incubated with indicated antibodies in indicated strains. N = 3 independent experiments. (E)

945 Schematic representations of core and non-core regions on reforming NE in mitotic *C. elegans* embryo

946 and line scan analysis of LEM-2^mNG protein dynamics shown in (G). (F) Spinning disk confocal

947 images of endogenous LEM-2^mNG enrichment at 140 sec post anaphase onset. Yellow arrows, core

948 enrichment. Scale bars, 5 μm. (G) Left, Plot representing average + SEM of ratio of maximum

949 fluorescence intensity and non-core fluorescence signal measured in 20 sec intervals from anaphase onset

950 (t = 0) in indicated conditions, Middle, Plot representing average + replicates of maximum normalized

951 LEM:2^mNG fluorescence signal from plot on left in indicated conditions, Right, Plot representing time

952 of maximum fluorescence signal in indicated conditions. n = # of embryos.

**A** SP12:GFP (ER)

**B** Pronuclei appearance at -400s PC regression

**C**

**D**

**E**
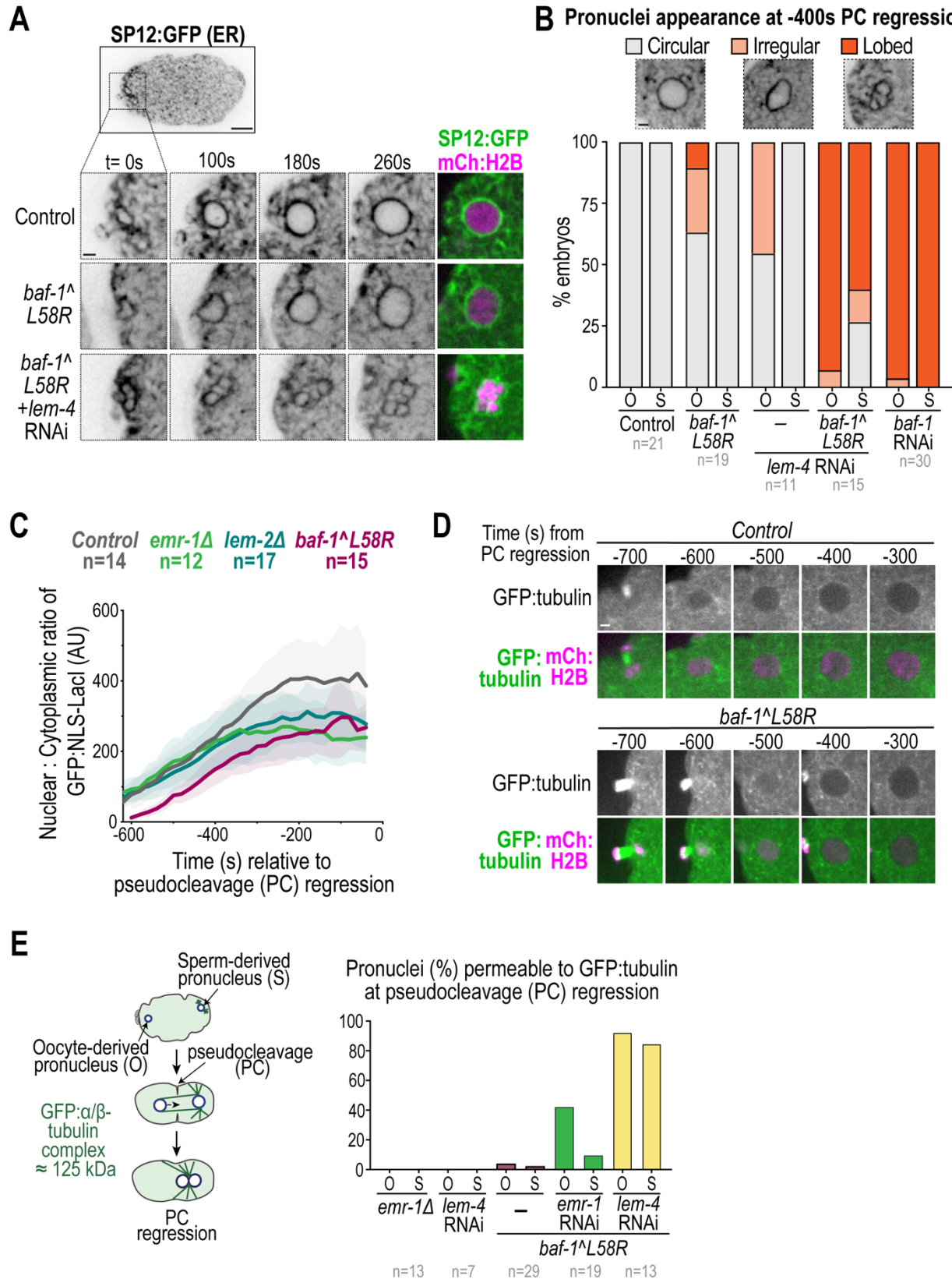
954 **Figure 4. Reliance on BAF-LEM binding to seal the NE large hole surrounding meiotic spindle**

955 **microtubules.** (A) Spinning disk confocal images from time lapse series of oocyte pronuclear formation

956 marked by SP12:GFP (ER marker) and mCh:Histone(H)2B in indicated conditions. (B) Plot representing

957 percentage of oocyte-derived (O) and sperm-derived (S) pronuclei categorized as circular, irregular, or

958 lobed at -400 sec relative to pseudocleavage (PC) regression in indicated conditions. n = # of embryos.

959 (C) Plot representing average ± SD of ratio of normalized GFP::NLS-LacI fluorescence in oocyte

960 pronucleus for indicated conditions relative to PC regression. n = # of embryos. (D) Spinning disk

961 confocal images from time-lapse series of nuclear GFP:$\alpha$-tubulin during oocyte pronuclear formation in

962 indicated conditions. Time in seconds relative to PC regression. (E) Left, schematic represents nulear

963 exclusion of GFP:$\alpha$-tubulin from pronuclei during pronuclear migration and pseudocleavage (PC)

964 formation and regression. Right, plot representing percentage of oocyte-derived (O) and sperm-derived

965 (S) pronuclei permeable to GFP:$\alpha$-tubulin at pseudocleavage regression. n = # of embryos. Scale bars, 2

966 μm.
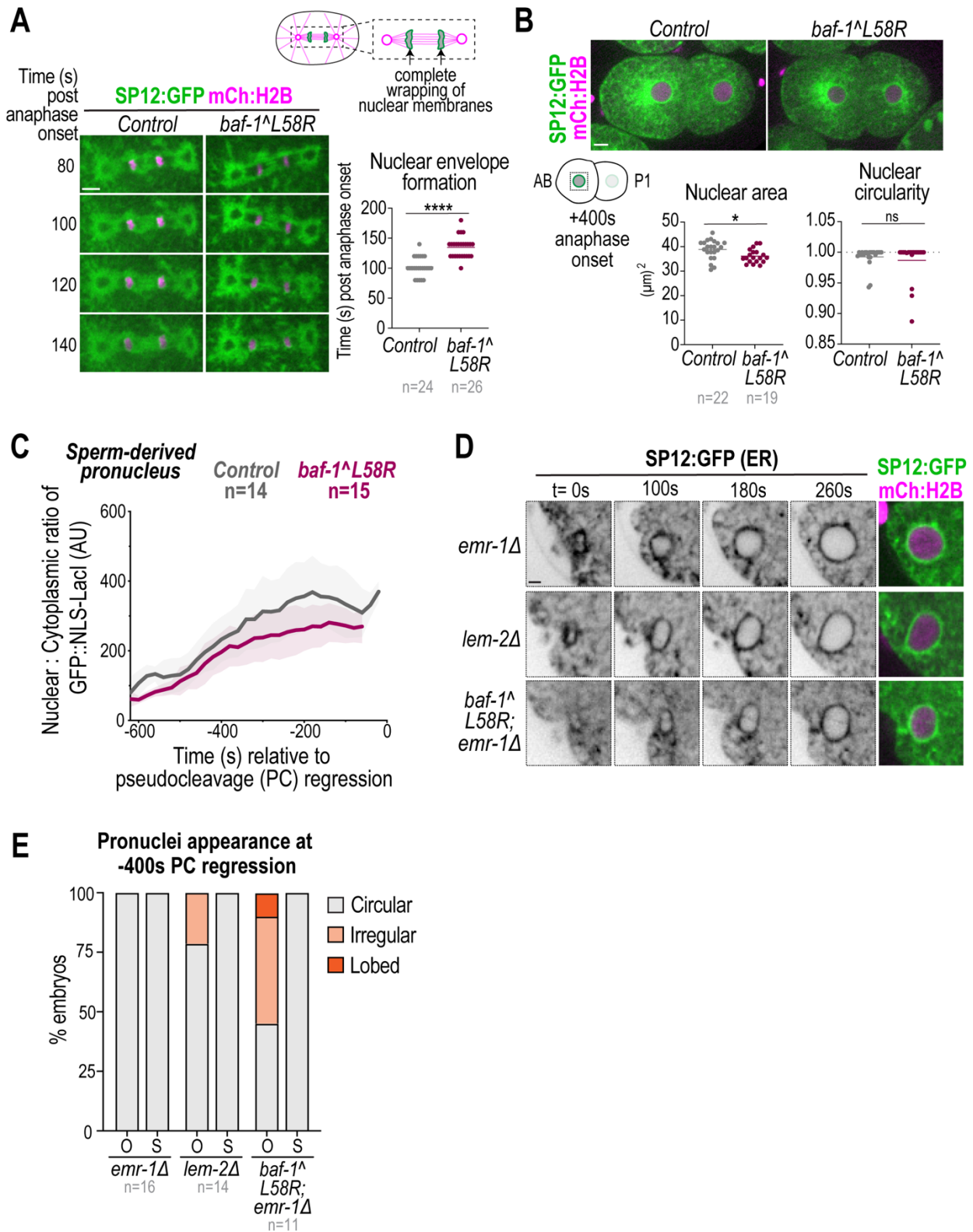
968 **Figure S4. Analysis of pronuclear assembly in *emr-1Δ* and *lem-2Δ* mutants**, related to Figure 4 (A)

969 Left, representative confocal images from time-lapse series of SP12:GFP (ER marker) and mCh:Histone

970 2B (DNA marker) in mitotic embryos in indicated conditions. Time in seconds relative to anaphase onset.

971 Right, plot representing average + replicates of time of complete wrapping of ER marker (SP12:GFP)

972 around segregated chromosomes in indicated conditions. Statistical significance determined by unpaired

973 Student's t-test (**** = p<0.0001). n = # of embryos. (B) Above, spinning disk confocal images of

974 indicated markers at 400 sec post anaphase onset in indicated conditions. Below, Schematic

975 representation of 2-cell embryo and plots representing average + replicates of AB cell nuclear area and

976 nuclear circularity at 400 sec post anaphase onset in indicated conditions. Statistical significance

977 determined by unpaired Student's t-test (* = p = 0.0149). ns, not significant. n = # of embryos. Scale bar,

978 5 μm. (C) Plot representing average ± SD of normalized nuclear GFP::NLS-LacI fluorescence in sperm-

979 derived pronucleus for indicated conditions. Time in seconds relative to pseudocleavage (PC) regression.

980 n = # of embryos. (D) Spinning disk confocal images from time lapse series of indicated markers during

981 oocyte-derived pronuclear formation in indicated conditions. Scale bar, 2 μm. (E) Plot representing

982 percentage of oocyte-derived (O) and sperm-derived (S) pronuclei categorized as circular, irregular, or

983 lobed at -400 sec relative to pseudocleavage (PC) regression in indicated conditions. n = # of embryos.

984
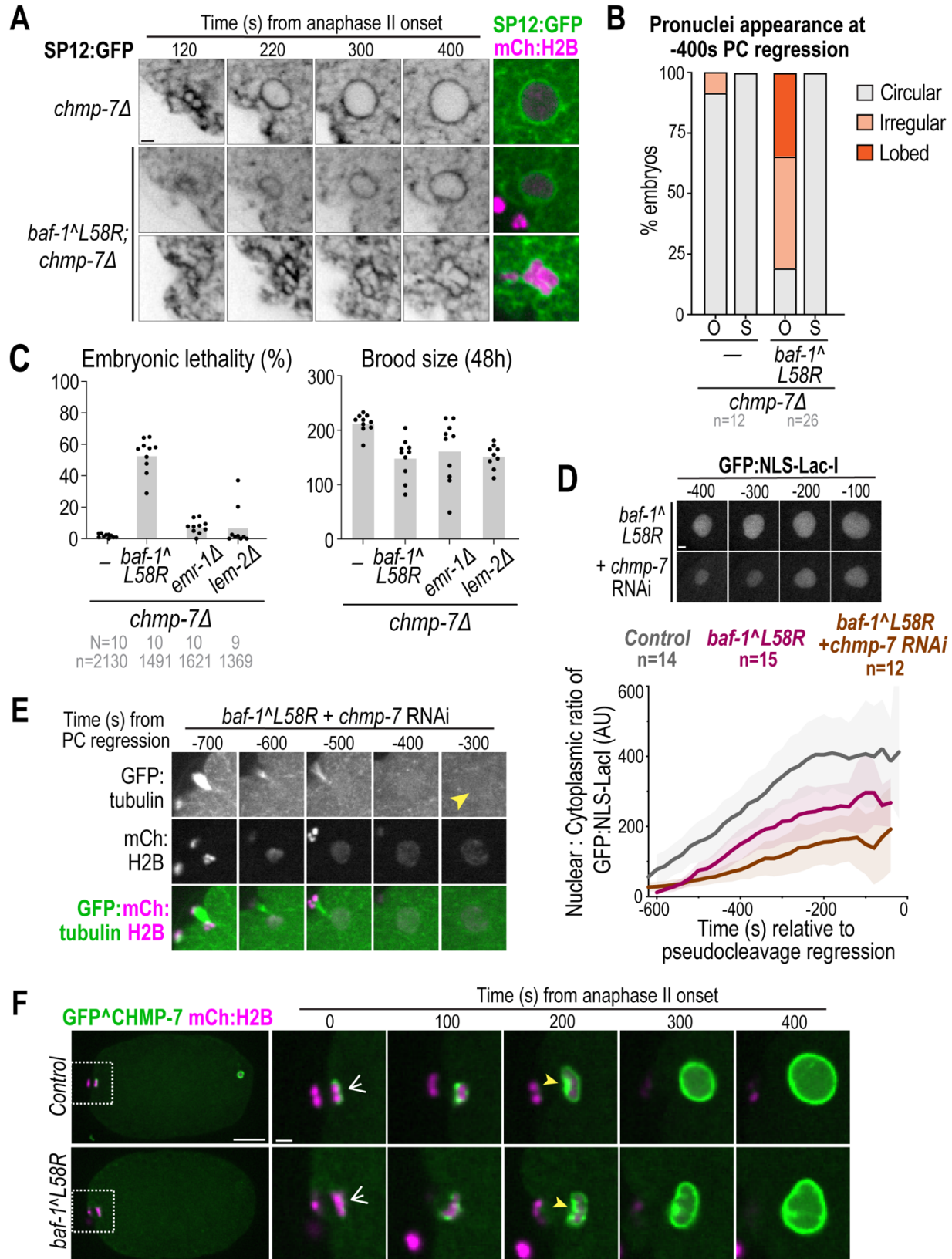
985 **Figure 5. CHMP-7 maintains nuclear integrity when BAF-LEM-mediated hole closure is**

986 **compromised.** (A) Spinning disk confocal images from time lapse series of SP12:GFP (ER) and

987 mCH:Histone(H)2B in indicated conditions during oocyte-derived pronuclear formation. (B) Plot

988 representing percentage of oocyte-derived (O) and sperm-derived (S) pronuclei categorized as circular,

989 irregular, or lobed at -400 sec relative to pseudocleavage (PC) regression in indicated conditions. n = # of

990 embryos. (C) Plots representing average + replicates of percentage of embryonic lethality and brood size

991 in indicated conditions. N = # of worms, n = # of embryos. (D) Plot representing average ± SD of

992 normalized nuclear GFP:NLS-LacI fluorescence in indicated conditions. Time in seconds relative to

993 pseudocleavage (PC) regression. Control and *baf-1-L58R* replicated from Fig. 4C. n = # of embryos. (E)

994 Spinning disk confocal images from time-lapse series of GFP-α-tubulin in the oocyte-derive pronucleus

995 in indicated conditions. Time in seconds relative to PC regression. Yellow arrow marks nuclear GFP-α-

996 tubulin. (F) Spinning disk confocal images from time lapse series of mNG^CHMP-7 during oocyte

997 pronuclear formation in indicated conditions. White arrows denote initial recruitment of GFP^CHMP-7 to

998 chromatin and yellow arrows point to enrichment. Time in seconds relative to anaphase II onset. Scale

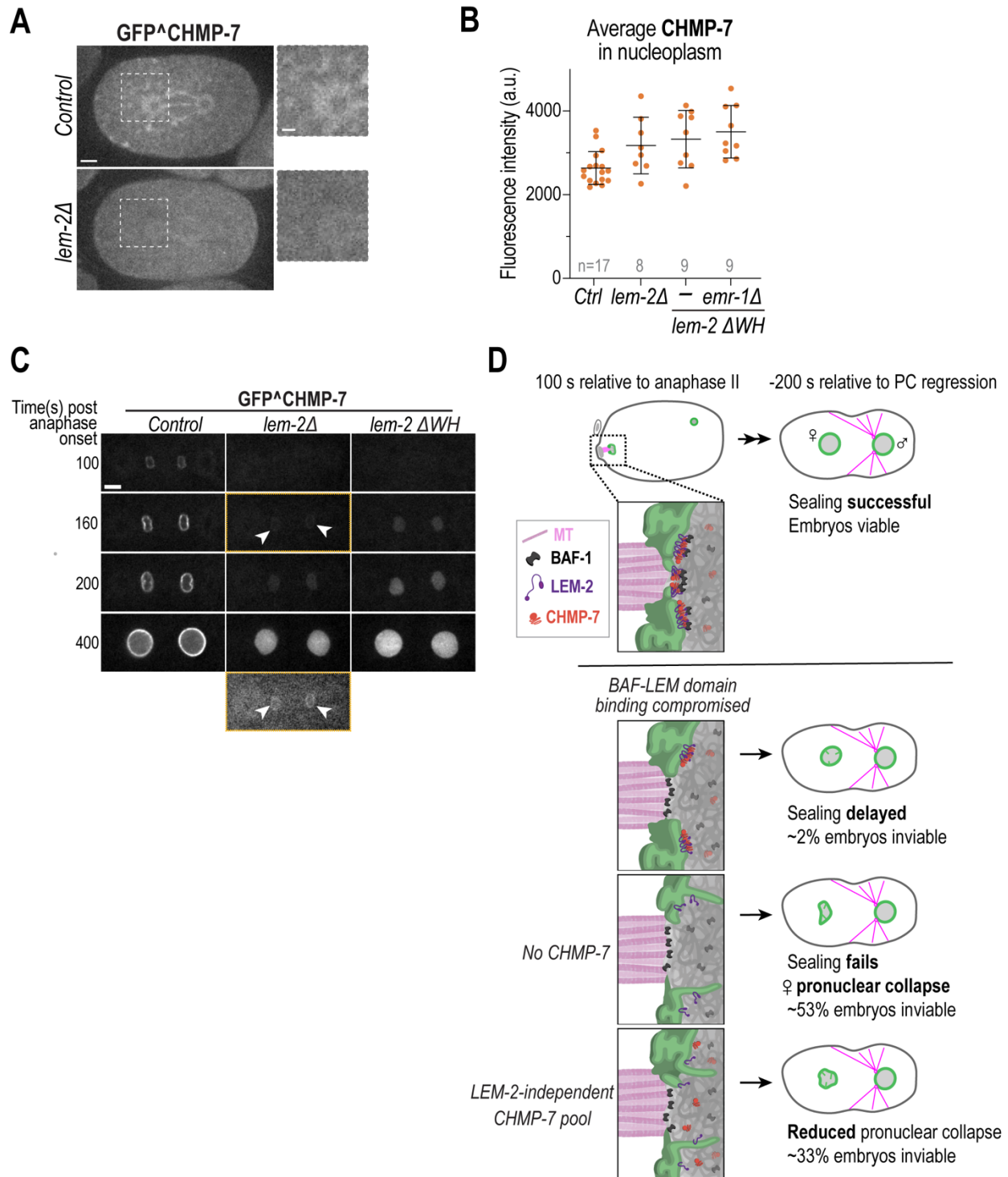999 bars of whole embryo images, 10 μm, all other scale bars, 2 μm.

44
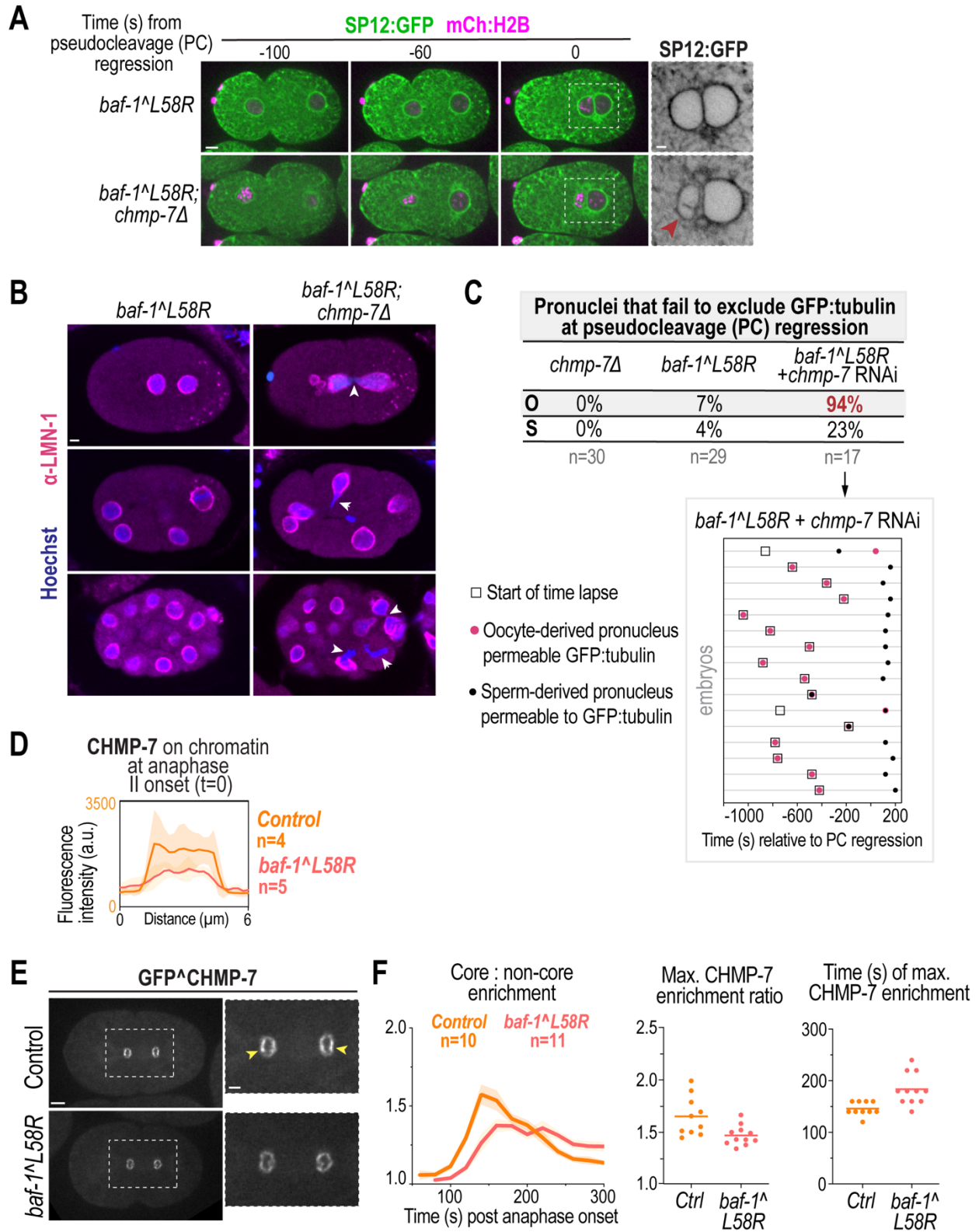
1001 **Figure S5. Analysis of loss of CHMP-7 and mNG^CHMP7 dynamics in meiosis and mitosis in *baf-***

1002 ***1-L58R* mutant embryos**, related to Figure 5 (A) Spinning disk confocal images from time lapse series

1003 of indicated markers in indicated conditions. Time in seconds relative to pseudocleavage (PC) regression.

1004 Scale bar, 5 μm, zoom inset image scale bar, 2 μm. (B) Confocal images of fixed 2-,8-,16+ -cell stage *C.*

1005 *elegans* embryos immunostained with indicated markers (LMN-1 = lamin) in indicated conditions. White

1006 arrows, chromatin bridges and impaired nuclear assembly. (C) Above, table showing percentage of

1007 oocyte-derived (O) and sperm-derived (S) pronuclei permeable to GFP:α-tubulin at pseudocleavage (PC)

1008 regression in indicated conditions. n = # of embryos. Below, Plot representing time points for individual

1009 embryos containing nuclear GFP:α-tubulin in oocyte- (red circles) or sperm-derived pronuclei (black

1010 circles) relative to start of time-lapse movie (square). Time in seconds relative to pseudocleavage (PC)

1011 regression. (D) Background-corrected line scan analysis (average ± SD) of GFP^CHMP-7 on the nuclear

1012 rim anaphase II onset (white arrows in Figure 5F) in indicated conditions. n = # of embryos. (E) Spinning

1013 disk confocal images of GFP^CHMP-7 at mitotic nuclear formation at 140 sec post anaphase onset.

1014 Yellow arrows, core domain. Scale bars, 5 μm. (F) Left, Plot representing average + SEM of ratio of

1015 maximum fluorescence intensity and non-core fluorescence signal measured in 20 sec intervals from

1016 anaphase onset (t = 0) in indicated conditions, Middle, Plot representing average + replicates of maximum

1017 normalized GFP^CHMP-7 fluorescence signal from plot on left in indicated conditions. Right, Plot

1018 representing time of maximum fluorescence signal in indicated conditions. n = # of embryos.

1019 n = # of embryos.

46

1020
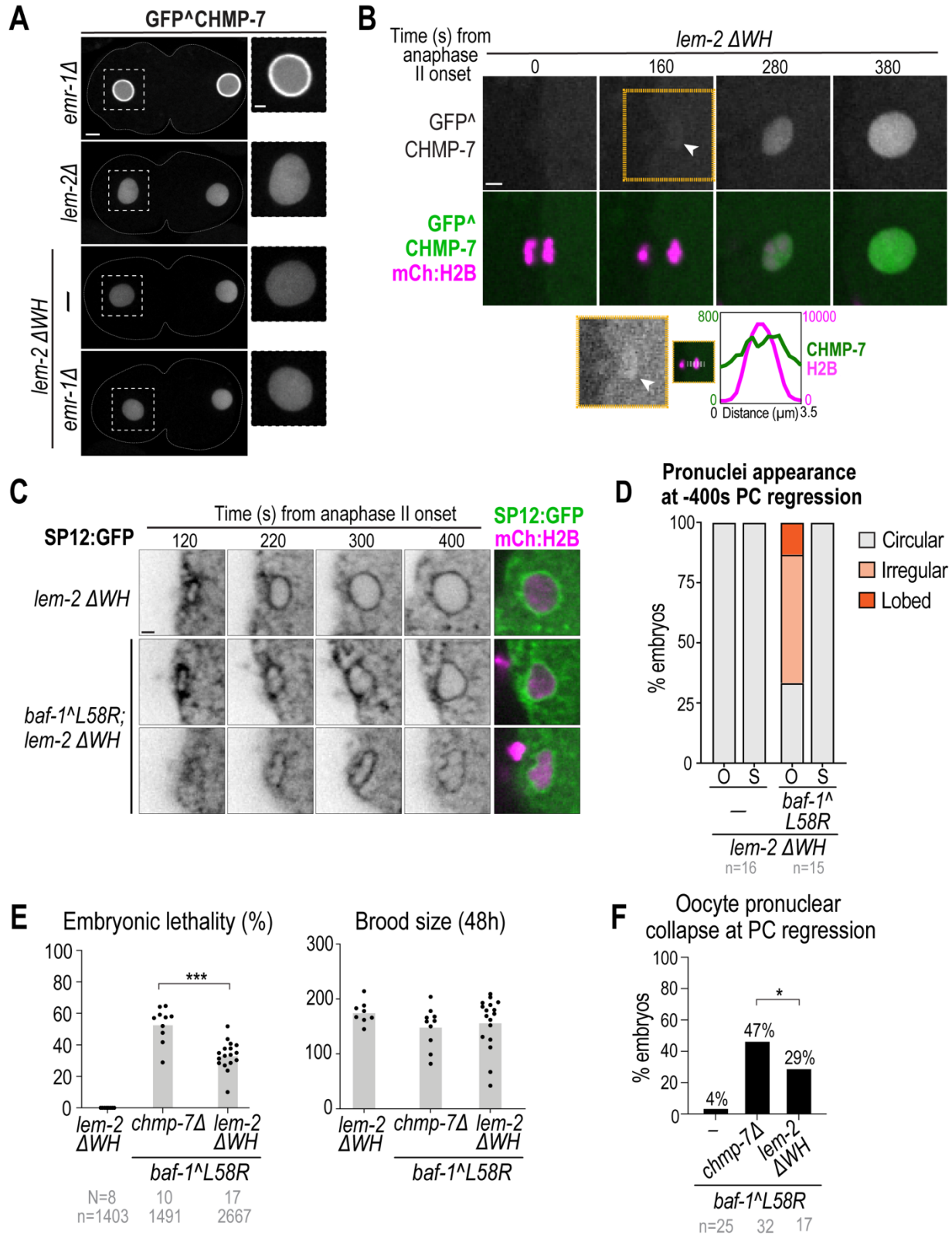
1021 **Figure 6. Compromising BAF-LEM binding reveals a role for CHMP-7 in nuclear stability**

1022 **independent of LEM-2 binding.** (A) Left, Spinning disk confocal images of GFP^CHMP-7 in embryos

1023 at -200 sec relative to pseudocleavage (PC) regression in indicated conditions. Scale bars, 5 μm, zoom

1024 scale bars, 2 μm. (B) Spinning disk confocal images from time lapse series of GFP^CHMP-7 and

1025 mCH:Histone(H)2B during oocyte pronuclear formation in *lem-2 ΔWH* embryos. Time is in seconds

1026 relative to anaphase II onset. White arrow denotes faint membrane-association of GFP^CHMP7 prior to

1027 nuclear enrichment. Yellow outlined panel reproduced below montage with brightness/contrast adjusted.

1028 Plot represents background-corrected line scan of fluorescence of GFP^CHMP-7 and mCH:Histone(H)2B

1029 across reforming nucleus at 160 s post anaphase II onset. (C) Spinning disk confocal images from time

1030 lapse series of indicated markers in indicated conditions. (D) Plot representing percentage of oocyte-

1031 derived (O) and sperm-derived (S) pronuclei categorized as circular, irregular, or lobed at -400 sec

1032 relative to PC regression in indicated conditions. n = # of embryos. (E) Plots representing average +

1033 replicates of percentage of embryonic lethality and brood size in indicated conditions. N = # of worms, n

1034 = # of embryos. Statistical significance of indicated conditions determined by Welch's t-test

1035 (***=p=0.0002). (F) Plot representing percentage of embryos that undergo oocyte pronuclear collapse in

1036 indicated conditions. n = # of embryos. Statistical significance of indicated conditions determined by

1037 Fisher's exact test (*=p=0.0130).

**Figure S6. CHMP-7 localization and dependence on LEM-2**, related to Figure 6 (A) Spinning disk confocal images of endogenous GFP^CHMP-7 in control and *lem-2Δ* embryos at anaphase onset in mitotic embryos. Zoom inset of spindle pole. Scale bar, 5 μm, zoom scale bar, 2 μm. (B) Plot representing

49

1043      average ± SD + replicates of nucleoplasmic GFP^ CHMP-7 levels in oocyte-derived pronuclei -200 sec

1044      relative to pseudocleavage (PC) regression. n = # of embryos. (C) Spinning disk confocal images from

1045      time series of GFP^CHMP-7 in indicated conditions. Time in seconds relative to anaphase onset. Scale

1046      bar, 5 μm. White arrowheads point to faint fluorescence signal of GFP^CHMP-7 prior to nuclear

1047      accumulation. Yellow outlined panel reproduced below with brightness/contrast adjusted. (D) Schematic

1048      representation of oocyte-derived pronuclear sealing in different mutant backgrounds analyzed in this

1049      study (left). Right, zoom inset of sealing plaque adjacent to spindle microtubules. LEM domain proteins

1050      (only LEM-2 is shown for simplicity) attach incoming ER membranes to BAF to narrow the nuclear

1051      envelope hole. CHMP-7/LEM-2 stabilize the nuclear envelope hole and remodel abnormal membranes,

1052      while a LEM-2 independent pool of CHMP-7 promotes nuclear stability through an unknown mechanism.

1053

1054      **Supplemental Movie Legends**

1055

1056      **Movie S1. BAF-1 dynamics at oocyte- and sperm-derived pronuclei during pronuclear formation,**

1057      related to Figure 1. Spinning disk confocal fluorescence time series of mNG^BAF-1 (green) and

1058      mCherry:Histone2B (magenta) in fertilized oocyte. Time lapse shows mNG^BAF-1 enrichment on

1059      chromatin transitioning to nuclear membranes during oocyte- (left) and sperm- (right) derived pronuclear

1060      formation. Images were acquired every 20 s – playback rate is 80X real time. Scale bar, 5 μm.

1061

1062      **Movie S2. BAF-1 is required for LEM-2 enrichment at the sealing plaque following meiosis II,**

1063      related to Figure 1. Spinning disk confocal fluorescence time series of endogenously tagged LEM-

1064      2^mNG (green) and mCherry:Histone2B (magenta) in fertilized oocytes. Time lapse shows oocyte-

1065      derived pronuclear formation, starting at anaphase II onset, as chromatin moves away from the cortex,

1066      and ending with a sealed pronucleus in indicated conditions. LEM-2^mNG does not accumulate at a

1067      discrete focus in the reforming oocyte-derived pronucleus, which undergoes assembly failure. Images

1068      were acquired every 20 s – playback rate is 80X real time. Scale bar, 2 μm.

1069

1070      **Movie S3. Reduced and delayed LEM-2^mNG enrichment at the sealing plaque in *baf-1^L58R***

1071      **embryos,** related to Figure 3. Spinning disk confocal fluorescence images of LEM-2^mNG (green) and

1072      mCherry:Histone2B (magenta) in fertilized oocytes in indicated conditions. Time lapse shows oocyte-

1073      derived pronuclear formation, starting at anaphase II onset. Images were acquired every 20 s – playback

1074      rate is 80X real time. Scale bar, 2 μm.

1075

1076 **Movie S4. Oocyte pronuclear formation in control, *baf-1^L58R*, *baf-1^L58R* + *lem-4* RNAi**

1077 **embryos,** related to Figure 4. Spinning disk confocal fluorescence time series of embryos expressing

1078 SP12:GFP (ER in grey, inverted) in indicated conditions. Images were acquired every 20 s – playback

1079 rate is 80X real time. Scale bar, 2 μm.

1080

1081 **Movie S5. Oocyte pronuclear collapse occurs in *chmp-7Δ*; *baf-1^L58R* embryos,** related to Figure 5.

1082 Spinning disk confocal fluorescence time series of SP12:GFP (ER, green) and mCherry:Histone2B

1083 (magenta) marking oocyte-derived pronuclei in indicated conditions. Time lapse shows migration of

1084 oocyte- and sperm-derived pronuclei ending in pronuclear meeting approximately at PC regression.

1085 Images were acquired every 20 s – playback rate is 80X real time. Scale bar, 5 μm.

1086

1087 **Movie S6. Reduced and delayed CHMP-7 enrichment at the sealing plaque in *baf-1^L58R* embryos,**

1088 related to Figure 5. Spinning disk confocal fluorescence time series of GFP^CHMP-7 (green) and

1089 mCherry:Histone2B (magenta) after anaphase II onset in fertilized oocytes in indicated conditions. Time

1090 lapse shows oocyte-derived pronuclear formation, starting at anaphase II onset as chromatin moves away

1091 from the cortex and ending with a formed pronucleus in indicated conditions. Images were acquired every

1092 20s – playback rate is 80X real time. Scale bar, 2 μm.

1093

1094 **Movie S7. Reliance of GFP^CHMP-7 on the Winged Helix domain of LEM-2 to localize and enrich**

1095 **at the sealing plaque following meiosis II,** related to Figure 6. Spinning disk confocal fluorescence time

1096 series of GFP^CHMP-7 (green) and mCherry:Histone2B (magenta) after anaphase II onset in fertilized

1097 oocytes in indicated conditions. Left, gray scale images of GFP^CHMP-7, Right, merged. Time lapse

1098 shows oocyte-derived pronuclear formation, starting at anaphase II onset as chromatin moves away from

1099 the cortex and ending with a formed pronucleus in *lem-2 ΔWH* mutant. Left, GFP^CHMP-7 (grey), Right,

1100 merged. Images were acquired every 20 s – playback rate is 80X real time. Scale bar, 2 μm.

1101

1102

1103    Table S1. *C. elegans* strains used in this study

1104

| *C. elegans* strain name | Genotype | Source |
|---|---|---|
| N2 | *(*Bristol): Wild-type (ancestral) | Caenorhabditis Genetics Center (CGC) |
| SBW69 | unc-119 (ed3) III; sbwSi6 [mex-5p::baf-1(re-encoded)::tbb-2]; cb-unc-119(+) I | This study |
| SBW130 | unc-119 (ed3) III; sbwSi12 [mex-5p::baf-1(re-encoded)-G47E::tbb-2 3']; cb-unc-119(+) I | This study |
| SBW131 | unc-119 (ed3) III; sbwSi13 [mex-5p::baf-1(re-encoded)-L58R::tbb-2 3' UTR)]; cb-unc-119(+) I | This study |
| SBW144 | baf-1(syb2609) III | This study; Suny Biotech |
| SBW136 | mNG::3XFlag::baf-1(sbw7) III | This study |
| SBW142 | mNG::3XFlag::baf-1(sbw7) III; unc-119(ed3) III; ltIs37 [pAA64; pie-1p::mCherry::his-58; unc-119 (+)] IV | This study |
| SBW152 | mNG::3XFlag::baf-1(sbw7) III; weIs21 [pJA138 (pie-1p::mCherry::tubulin::pie-1)] | This study |
| SBW198 | mNG::3XFlag::baf-1(L58R) III. [+/-] | This study |
| SBW253 | emr-1(gk119) I; mNG::3XFlag::baf-1(sbw7) III; unc-119(ed3) III; ltIs37 [pAA64; pie-1p::mCherry::his-58; unc-119 (+)] IV. | This study |
| VC237 | emr-1(gk119) I | Caenorhabditis Genetics Center (CGC) |
| SBW448 | lem-2 (sbw20) II | This study |
| TG4319 | lem-3(tm3468) I | Caenorhabditis Genetics Center (CGC) |
| SBW174 | emr-1(gk119) I; baf-1(syb2609) III | This study |
| SBW180 | lem-3(tm3468) I; baf-1(syb2609) III | This study |

| SBW47 | unc-119(ed3) III; ltIs37 [pAA64; pie-1p::mCherry::his-58; unc-119 (+)] IV; ltIs75 [(pSK5) pie-1::GFP::TEV-STag::LacI + unc-119(+)]. | (Audhya et al., 2007) |
|---|---|---|
| SBW170 | baf-1(syb2609) III ; unc-119(ed3) III; ltIs37 [pAA64; pie-1p::mCherry::his-58; unc-119 (+)] IV; ltIs75 [(pSK5) pie-1::GFP::TEV-STag::LacI + unc-119(+)]. | This study |
| SBW181 | emr-1(gk119) I; unc-119(ed3) III; ltIs37 [pAA64; pie-1p::mCherry::his-58; unc-119 (+)] IV; ltIs75 [(pSK5) pie-1::GFP::TEV-STag::LacI + unc-119(+)]. | This study |
| SBW457 | lem-2 (sbw20) I ; unc-119(ed3) III; ltIs37 [pAA64; pie-1p::mCherry::his-58; unc-119 (+)] IV; ltIs75 [(pSK5) pie-1::GFP::TEV-STag::LacI + unc-119 (+)]. | This study |
| OD270 | unc-119(ed3) III; ojIs23 [SP12::GFP; unc-119(+)]; ltIs37 [pAA64; pie-1p::mCherry::his-58; unc-119 (+)] | (Bahmanyar et al., 2014) |
| SBW173 | baf-1(syb2609) III; ojIs23 [SP12::GFP; unc-119(+)]; ltIs37 [pAA64; pie-1p::mCherry::his-58; unc-119 (+)] IV | This study |
| SBW199 | emr-1(gk119) I ; ojIs23 [SP12::GFP; unc-119(+)]; ltIs37 [pAA64; pie-1p::mCherry::his-58; unc-119 (+)] IV | This study |
| SBW543 | lem-2 (sbw20) II ; ojIs23 [SP12::GFP; unc-119(+)]; ltIs37 [pAA64; pie-1p::mCherry::his-58; unc-119 (+)] IV | This study |
| SBW32 | ltIs24 [pAZ132; pie-1p::GFP::tba-2; unc-119 (+)]; ltIs37 [pAA64; pie-1p::mCherry::his-58; unc-119 (+)] IV | (Penfield et al., 2018) |
| SBW171 | baf-1(syb2609) III; ltIs24 [pAZ132; pie-1p::GFP::tba-2; unc-119 (+)]; ltIs37 [pAA64; pie-1p::mCherry::his-58; unc-119 (+)] IV | This study |
| SBW480 | emr-1(gk119) I; ltIs24 [pAZ132; pie-1p::GFP::tba-2; unc-119 (+)]; ltIs37 [pAA64; pie-1p::mCherry::his-58; unc-119 (+)] IV | This study |
| SBW146 | lem-2::mNG (sbw5) II; unc-119(ed3) III; ltIs37 [pAA64; pie-1p::mCherry::his-58; unc-119 (+)] IV. | This study |
| SBW206 | lem-2::mNG (sbw5) II; baf-1(syb2609) III; unc-119(ed3) III; ltIs37 [pAA64; pie-1p::mCherry::his-58; unc-119 (+)] IV | This study |
| SBW414 | gfp::chmp-7 II; unc-119(ed3) III; ltIs37 [pAA64 pie-1p::mCherry::his-58; unc-119 (+)] IV | This study |

| SBW428 | gfp::chmp-7 II; baf-1(syb2609) III ; unc-119(ed3) III; ltIs37 [pAA64; pie-1p::mCherry::his-58; unc-119 (+)] IV | This study |
|---|---|---|
| SBW312 | mNG::3xFlag::emr-1 (sbw16) I. outcrossed 4X; unc-119(ed3) III; ltIs37 [pAA64; pie-1p::mCherry::his-58; unc-119 (+)] IV | This study |
| SBW350 | mNG::3xFlag::emr-1 (sbw16) I ; baf-1(syb2609) III ; unc-119(ed3) III; ltIs37 [pAA64; pie-1p::mCherry::his-58; unc-119 (+)] IV. | This study |
| SBW161 | chmp-7(hz12) II; unc-119(ed3) III; ojls23[SP12::GFP unc-119(+)]; unc-119(ed3) III; ltIs37 [pAA64; pie-1p::mCherry::his-58; unc-119 (+)] IV | This study |
| SBW196 | chmp-7(hz12) II; baf-1(syb2609) III; unc-119(ed3) III; ojls23 [SP12::GFP; unc-119(+); ltIs37 [pAA64; pie-1p::mCherry::his-58; unc-119 (+)] IV | This study |
| SBW63 | chmp-7(hz12) II; ltIs24 [pAZ132; pie-1p::GFP::tba-2; unc-119 (+)]; ltIs37 [pAA64; pie-1p::mCherry::his-58; unc-119 (+)] IV | (Penfield et al., 2020) |
| SBW526 | emr-1(gk119) I; gfp::chmp-7 II; unc-119(ed3) III; ltIs37 [pAA64; pie-1p::mCherry::his-58; unc-119 (+)] IV | This study |
| SBW458 | lem-2 (sbw20) II; gfp::chmp-7 II; unc-119(ed3) III; ltIs37 [pAA64; pie-1p::mCherry::his-58; unc-119 (+)] IV | This study |
| SBW419 | gfp::chmp-7 II; lem-2 (syb4718) II; unc-119(ed3) III; ltIs37 [pAA64; pie-1p::mCherry::his-58; unc-119 (+)] IV | This study |
| SBW547 | emr-1(gk119) I; gfp::chmp-7 II; lem-2 (syb4718) II; unc-119(ed3) III; ltIs37 [pAA64; pie-1p::mCherry::his-58; unc-119 (+)] IV | This study |
| SBW332 | lem-2 (syb4718) II; ojls23 [SP12::GFP; unc-119(+)]; ltIs37 [pAA64; pie-1p::mCherry::his-58; unc-119 (+)] IV | This study |
| SBW536 | lem-2 (syb4718) II; baf-1(syb2609) III; ojls23 [SP12::GFP; unc-119(+)]; ltIs37 [pAA64; pie-1p::mCherry::his-58; unc-119 (+)] IV | This study |
| MSN772 | chmp-7(hz12) II | (Penfield et al., 2020) |
| SBW168 | chmp-7(hz12) II; baf-1(syb2609) III | This study |
| SBW454 | emr-1(gk119) I; chmp-7(hz12) II | This study |

| SBW450 | lem-2 (sbw20) II; chmp-7(hz12) II | This study |
|--------|-----------------------------------|------------|
| SBW319 | lem-2 (syb4718) II | This study; Suny Biotech |
| SBW348 | lem-2 (syb4718) II; baf-1(syb2609) III | This study |

1105

1106

1107

1108

1109

1110

1111

1112
1113
1114
1115
1116
1117
1118
1119
1120
1121
1122
1123
1124
1125
1126
1127
1128
1129
1130
1131
1132
1133
1134
1135
1136
1137
1138

1139 Table S2. Oligonucleotides used in this study.
1140

| Purpose | Primers |
|---|---|
| pCFJ151-baf-1-G47E mutagenesis-Forward | GCCTACGTCTTGTTCGAACAGTATCTCCTGCTT |
| pCFJ151-baf-1-G47E mutagenesis-Reverse | AAGCAGGAGATACTGTTCGAACAAGACGTAGGC |
| pCFJ151-baf-1-L58R mutagenesis-Forward | AAAAAGGATGAGGATCGTTTCATCGAGTGGCTG |
| pCFJ151-baf-1-L58R mutagenesis-Reverse | CAGCCACTCGATGAAACGATCCTCATCCTTTTT |
| | |
| **Oligonucleotides for dsRNA production** | | | |

| Gene | Oligonucleotide 1 | Oligonucleotide 1 | Template |
|---|---|---|---|
| B0464.7 (*baf-1*) | TAATACGACTCACTATAGGCATCGTGAGTTCGTCGGAGA | TAATACGACTCACTATAGGgtccaagaccacacgacaag | N2 genomic |
| Y55F3BR.8 (*lem-4*) | TAATACGACTCACTATAGGCCGAGCAATCAGAAGCCATG | TAATACGACTCACTATAGGTTGCATGGCTCATCATCTGC | N2 genomic |
| T24B8.2 (*chmp-7*) | TAATACGACTCACTATAGGTCGGTGAATGGAGAGATCGT | TAATACGACTCACTATAGGGTTCTGAGCACGTCCTTTGT | N2 genomic |
| M01D7.6 (*emr-1)* | AATTAACCCTCACTAAAGGCGAACTACGCGATAGCCTTA | TAATACGACTCACTATAGGCCCAAGAATCCTCCTTTGTT | N2 genomic |

1141
1142
1143
1144
1145
1146
1147
1148
1149
1150
1151
1152
1153
1154
1155
1156
1157
1158
1159

1160    Table S3. Recombinant DNA used in this study.
1161

| Identifier | Recombinant DNA | Source |
|---|---|---|
|  | baf-1 re-encoded | Genescript |
| pSB353 | pCFJ151-baf-1-WT reencoded | This study |
| pSB419 | pCFJ151-baf-1-G47E reencoded | This study |
| pSB420 | pCFJ151-baf-1-L58R reencoded | This study |
|  | pDD122 (CRISPR-Cas9) | (Hastie et al., 2019) |
|  | pDD268 (mNG^SEC^3xFlag vector with ccdB markers for cloning homology arms) | Addgene (132523) |
|  | pBS-LL-mNG | (Hastie et al., 2019) |
| pSB457 | pDD122-lem-2 | This study |
| pSB462 | lem-2-LL-mNG | This study |
| pSB495 | pDD122-baf-1 | This study |
| pSB496 | pDD268-baf-1 | This study |
| pSB514 | pDD122-emr-1 | This study |
| pSB651 | pDD268-emr-1 | This study |

1162
1163
1164